A&A, 712, A99 (2026)
https://doi.org/10.1051/0004-6361/202556989

Astronomy & Astrophysics

The seven dwarfs illuminated

The impact of radiation on dwarf galaxies and their circumgalactic medium

Bernhard Baumschlager[1,⋆], Sijing Shen[1], James W. Wadsley[2], Benjamin Keller[3], Robert Wissing[1], Lucio Mayer[4], Piero Madau[5], Ferah Munshi[6], and Alyson Brooks[7]

[1] Institute of Theoretical Astrophysics, University of Oslo, PO Box 1029 Blindern, 0315 Oslo, Norway
[2] Department of Physics and Astronomy, McMaster University, Hamilton L8S 4M1, Canada
[3] Department of Physics and Material Science, University of Menphis, 3720 Alumni Avenue, Memphis, TN 38152, USA
[4] Department of Astrophysics, University of Zurich, Winterthurerstrasse 190, 8057 Zurich, Switzerland
[5] Department of Astronomy & Astrophysics, University of California, 1156 High Street, Santa Cruz, CA 95064, USA
[6] Department of Physics & Astronomy, George Mason University, 4400 University Drive, Fairfax, VA 22030, USA
[7] Department of Physics and Astronomy, Rutgers University, the State University of New Jersey, 136 Frelinghuysen Road, Piscataway, NJ 08854-8019, USA

Received 26 August 2025 / Accepted 10 March 2026

ABSTRACT

We present a high-resolution cosmological zoom-in simulation of a group of field dwarf galaxies that includes on-the-fly radiative transfer (RT) and is evolved to $z = 0$. Emission from stars is included according to age-dependent spectral energy distributions, and a redshift-dependent UV background is modelled by background particles and propagated through the simulation volume. The simulation also incorporates star formation, supernova (SN) feedback, a non-equilibrium primordial chemical network, and metal cooling and diffusion. We compare results from this simulation to previous simulations with the same initial conditions and largely similar galaxy formation physics, but without RT. The inclusion of RT results in the formation of eight additional faint dwarf galaxies with stellar masses of 10^4 $M_{\odot}$ to several 10^5 $M_{\odot}$ and only old stellar populations, similar to the observed ultra-faint dwarf galaxies. These eight faint dwarf galaxies formed before and during cosmic reionisation and were mostly quenched by $z \sim 3$–4 when reionisation was complete. The simulated galaxies follow many observed scaling relations such as the stellar mass-halo mass relation, the mass-size relation, and the luminosity-velocity dispersion relation. However, the simulation appears to underpredict the stellar iron abundances for the faintest population with $L_{\rm v} < 10^6 L_{\odot}$. For the more massive "classic" dwarf galaxies, radiative feedback suppresses star formation, making it less bursty and reducing explosive outflows. This consequently reduces the dark matter core sizes by a factor of two to three, rendering the core sizes (~1 kpc) more consistent with observations. The distribution of neutral hydrogen H I in the circumgalactic medium (CGM) is ubiquitous, with a covering fraction of unity within $R_{\rm vir}$, and in good agreement with observations. It is rather insensitive to radiative or SN feedback at $z = 0$, but at $z > 5$, it is much higher in the RT simulation. In contrast, the distribution of low-ionisation species such as Si II is very compact and declines sharply beyond the interstellar medium (ISM) scale. C IV and O VI have a more extended distribution, but their column densities are generally below the detection limit. Radiative feedback leads to smaller column densities of the metal ions, partly due to the reduction of total metal production, and partly because hard photons from the stellar radiation escape the ISM and further ionise the CGM. The abundance of C IV is particularly sensitive to the latter effect.

Key words. radiative transfer – methods: numerical – galaxies: dwarf – galaxies: evolution – galaxies: formation – galaxies: ISM

1. Introduction

Dwarf galaxies constitute the low mass end of the galaxy zoo and are the most numerous and least luminous systems in the Universe. In the framework of hierarchical structure formation of the Λ cold dark matter (CDM) paradigm, dwarf galaxies form within the earliest collapsing halos and become the building blocks for more massive galaxies. Observations of dwarf galaxies have posed significant challenges to the ΛCDM model. For example, simulations predict that Milky Way-mass halos should host significantly more satellite galaxies than observed around the Milky Way and M31. This discrepancy, known as the "missing satellite problem," suggests that either the predicted small halos fail to form stars or that many remain undetected (e.g. Moore et al. 1999; Klypin et al. 1999). Furthermore, dark matter (DM)-only simulations predict a cuspy inner DM profile, whereas observations of rotation curves of dwarf galaxies suggest that the DM profile is cored, i.e. has a near-constant inner slope, the so-called "cusp-core problem" (e.g. Flores & Primack 1994; Navarro et al. 1996; de Blok & Bosma 2002). Finally, the most massive subhalos in DM-only simulations of Milky Way-sized galaxies are too massive compared to observed Milky Way satellites; this is referred to as the "too-big-to-fail (TBTF) problem" (Boylan-Kolchin et al. 2011, 2012).

Although alternative DM models are invoked to alleviate these tensions (e.g. Vogelsberger et al. 2014; Fitts et al. 2019; Mina et al. 2022; Nori et al. 2024; Shen et al. 2024), many studies have shown that baryonic processes can also have a significant impact. Due to their shallow gravitational potential wells, dwarf galaxies are sensitive to mechanical and radiative feedback from stars and potentially active galactic nuclei (AGN) (e.g. Dashyan et al. 2018; Sharma et al. 2020; Koudmani et al. 2021, 2025). After reionisation, photoionisation heating from the cosmic ultraviolet background (UVB) suppresses gas accretion

⋆ Corresponding author: bernhard.baumschlager@astro.uio.no

into the small halos (e.g. Efstathiou 1992; Bullock et al. 2000; Dijkstra et al. 2004; Madau et al. 2008; Gutcke et al. 2022b), which alleviates the "missing satellite problem". Galactic outflows driven by stellar feedback can rapidly change the central gravitational potential wells, leading to cusp-core transformation (e.g. Mashchenko et al. 2008; Governato et al. 2010; Pontzen & Governato 2012; Madau et al. 2014; Fitts et al. 2017; Mostow et al. 2025). The cored DM profile reduces the peak velocity in galaxy rotation curves, which alleviates the TBTF problem (Zolotov et al. 2012; Brooks & Zolotov 2014; Wetzel et al. 2016).

Meanwhile, the inclusion of feedback is also crucial for modern hydrodynamic simulations of dwarf galaxies to successfully reproduce observed properties of Local Group dwarf galaxies, such as the stellar mass content (e.g. Behroozi et al. 2013; Moster et al. 2013; Brook et al. 2014; Garrison-Kimmel et al. 2014; Read et al. 2017), star formation history (SFH; e.g. Brown et al. 2014; Weisz et al. 2014), mass-metallicity relation (MZR; e.g. McConnachie 2012; Kirby et al. 2013), and stellar and gas kinematics (McConnachie 2012). One of the key processes is feedback-driven galactic outflows. Numerous studies have shown that galactic outflows are of critical importance in suppressing star formation, ejecting metals into the circumgalactic medium (CGM) and the intergalactic medium (IGM) and thus lowering stellar and gas metallicity in the disc and reducing the stellar bulge-to-disc ratio (e.g. Shen et al. 2014; Oñorbe et al. 2015; Wheeler et al. 2015; Fitts et al. 2017). Traditionally, supernova feedback is generally invoked in generating outflows, but it is still under debate whether supernovae alone are responsible for reproducing all the observed properties of local dwarf galaxies. This is partly because subgrid models are often adopted for supernova feedback, which can either overestimate or underestimate the supernova energy and momentum injection into the interstellar medium (ISM). Indeed, the properties of dwarf galaxies can be very sensitive to supernova feedback models, especially the outflow and CGM properties (e.g. Mina et al. 2021), and convergence between various models is achieved only with extreme resolution (e.g. Smith et al. 2018). More recently, cosmological simulations, such as EDGE (Agertz et al. 2020) and LYRA (Gutcke et al. 2021), were able to push to very high resolutions such that the Sedov–Taylor phase of the supernova explosion was largely resolved, and thus the momentum injection is not dependent on subgrid models. However, even in this case, results did not fully converge between the different numerical methods (Hu et al. 2023). Moreover, the impact of supernovae also depends on the ISM conditions and the baryonic cycle, and the interplay between supernova feedback and other physical processes, including gas accretion, turbulence, H_2 chemistry, star formation, magnetic fields, and possible AGN feedback, are non-linear and complex (e.g. Hu et al. 2016; Munshi et al. 2019; Agertz & Kravtsov 2015; Koudmani et al. 2021; Martin-Alvarez et al. 2023; Sharma et al. 2023; Arjona-Gálvez et al. 2024).

Radiation from stars and AGN is one of such processes that significantly impacts the condition of the ISM (and also the CGM and IGM, i.e. the entire baryonic cycle). As mentioned previously, cosmic reionisation directly affects the formation of the faintest galaxies by reducing or quenching gas accretion onto the smallest halos. At the ISM scale, detailed ISM simulations have shown that photoionising and photodissociating radiation from massive stars precedes supernova explosions and can significantly reduce the ISM densities where supernovae occur, thus boosting local supernova efficiency and wind launching (e.g. Walch & Naab 2015; Kim & Ostriker 2017; Peters et al. 2017). In addition to radiative heating, radiation pressure can directly inject momentum into the ISM and drive galactic winds itself, especially for starburst galaxies and active galaxies (Fabian 2012).

For galactic scale simulations and cosmological simulations, on-the-fly radiative transfer (RT) is computationally costly because of its requirements for spatial and temporal resolutions. However, great progress has been made in recent years, and fully coupled RT has become more feasible, for example, in simulations of the Epoch of Reionisation (EoR) such as CROC (Gnedin 2014), SPHINX (Rosdahl et al. 2018) and THESAN (Kannan et al. 2022; Borrow et al. 2023). Although these simulations are usually stopped at a high redshift (e.g. $z \sim 6$), the self-consistent modelling of the evolving UV background already revealed interesting results. For dwarf galaxy formation and quenching, the inhomogeneity of the ionising background and the timing of reionisation in a specific region can cause significant scatter in the SFH of small halos (Katz et al. 2020). Such an effect cannot be captured with the traditional approach in cosmological simulations, where a spatially uniform UVB is turned on instantaneously and is only a function of time. As for the interplay between radiation, supernova feedback, and star formation, isolated galaxy simulations (Rosdahl et al. 2015; Emerick et al. 2018; Smith et al. 2021; Deng et al. 2024) and cosmological zoom-in simulations (Agertz et al. 2020; Hopkins et al. 2020; Martin-Alvarez et al. 2023; Rey et al. 2025) with either full RT or ISM models that capture the impact of radiative feedback have both shown that radiative heating suppresses global star formation and stellar mass, but it is still unclear how the global supernova efficiency is affected. While some studies (Rosdahl et al. 2015; Hopkins et al. 2020; Smith et al. 2021; Deng et al. 2024; Rey et al. 2025) found that radiative heating prevents the formation of dense clouds and "smooths out" the ISM, resulting in a less bursty SFH and more gentle SN-driven outflows, others (e.g. Emerick et al. 2018) found the opposite, namely radiative feedback helps to create ISM conditions that favour supernova feedback, which is similar to what is found in small-scale ISM simulations. As rapid fluctuations of the central gravitational potential well are essential for the DM cusp-core transformation, it is expected that the burstiness of star formation will have an impact on DM core properties.

Observationally, with the advent of digital sky surveys and deep imaging, in the past two decades there has been a rapid growth of new discoveries of the faintest galaxy population, the ultra-faint dwarf galaxies (UFDs; e.g. Simon 2019; Richstein et al. 2024), typically with luminosities $L < 10^5\ L_\odot$. These galaxies have predominantly very early SFHs (e.g. Brown et al. 2014) and low metallicities (e.g. Fu et al. 2023), indicating that they are likely true relics of reionisation. As such, it is important to include radiative transport in simulations of UFDs. Moreover, their smaller mass and quiescent star formation activities today imply insufficient SN feedback and energy injection for the cusp-core transformation, making them ideal for breaking the degeneracy between alternative DM models and baryonic processes in the cusp-core problem (Governato et al. 2012). With recently launched missions such as the Euclid satellite (Euclid Collaboration 2025; Marleau et al. 2025) and Rubin Observatory (Ivezić et al. 2019), and future missions such as the Roman Space Telescope (Akeson et al. 2019) and Arrakihs (Corral van Damme et al. 2024), observations will continue to push the limit of detecting faint dwarf galaxies and low surface brightness features, which will significantly improve our understanding of DM and galaxy formation in general.

In addition to the stellar and ISM components, observations of the CGM can also reveal crucial information on the baryonic cycle, feedback, and environmental effects in dwarf galaxy formation. Observations of the CGM around nearby dwarf galaxies, mainly through absorption line studies (e.g. HST/COS), have reported that although neutral hydrogen (H I) is ubiquitous, detections of the low ionisation metal species such as C II and Si II are generally rare around dwarf galaxies, whereas detections of intermediate or highly ionised metal lines (e.g. C IV) are relatively more common but still less frequent than those around more massive galaxies (e.g. Prochaska et al. 2011; Bordoloi et al. 2014; Liang & Chen 2014; Burchett et al. 2016; Johnson et al. 2017; Zheng et al. 2020, 2024; Mishra et al. 2024). Because observations only probe ions rather than the total gas or metal mass, it is important to understand the role of the local radiation field on the ionisation states of the CGM. For simplicity, CGM analysis of cosmological simulations usually assumes uniform UVB radiation when post-processing simulations. While this may be a good approximation at large distances in the outer halo, it is inaccurate for the inner CGM, as local radiation can dominate the radiation field and impact ion abundances, at least for high-redshift, starburst galaxies (Shen et al. 2013), and Milky Way-type galaxies (Zhu & Springel 2024). It remains to be explored how the CGM of dwarf galaxies is affected by the local radiation field, and RT is an essential tool to investigate this topic.

Much effort has been devoted to simulating dwarf galaxy formation and evolution. In particular, cosmological zoom-in simulations of field dwarf galaxies (e.g. Governato et al. 2010; Shen et al. 2014; Oñorbe et al. 2015; Wheeler et al. 2015; Fitts et al. 2017; Jeon et al. 2017; Smith et al. 2018; Revaz & Jablonka 2018; Fitts et al. 2019; Munshi et al. 2019; Wright et al. 2019; Agertz et al. 2020; Gutcke et al. 2021; Mina et al. 2021; Martin-Alvarez et al. 2023; Azartash-Namin et al. 2024), and satellite dwarf galaxies around MW-like galaxies or in Local Group-like environments (e.g. Brooks & Zolotov 2014; Sawala et al. 2016; Wetzel et al. 2016; Santos-Santos et al. 2018; Applebaum et al. 2021) have achieved great success in reproducing the observed dwarf galaxy population in the local Universe, and in advancing our understanding of the key physics that shapes galaxy formation at the faintest end. More recent studies (e.g. Li et al. 2021; Mina et al. 2021; Piacitelli et al. 2025) have also investigated the CGM properties around dwarf galaxies at low redshift. However, full RT has only been included in such simulations more recently, for example, in EDGE (Agertz et al. 2020; Rey et al. 2025) and Pandora (Martin-Alvarez et al. 2023). These simulations, together with the RT EoR simulations, have shown the importance of modelling the UVB and local radiation field properly in dwarf galaxy formation. Nevertheless, due to computational cost and challenges, cosmological RT simulations often have to be terminated at a relatively high redshift, typically at $z > 3$, or focus on the smallest halos (typically with halo mass $M_\mathrm{h} \sim 10^9\,\mathrm{M}_\odot$) in an isolated environment, but observations of dwarf galaxies and the CGM are predominantly at the local Universe and in more massive systems. Therefore, it remains to be investigated how the impact of radiation evolves throughout cosmic history in various halo masses, how it interacts with star formation and supernova feedback, and how it affects cusp-core transformation and CGM ionisation states.

In this work, we explore these questions using a cosmological zoom-in simulation of a group of field dwarf galaxies with a host halo of mass $M_\mathrm{vir} \lesssim 10^{10.5}\,\mathrm{M}_\odot$ with on-the-fly RT evolved to $z = 0$. Radiative transfer is performed with a tree-based reverse ray tracing algorithm TREVR2 (Wadsley et al. 2024). The initial condition is adopted from the seven dwarfs simulation from Shen et al. (2014), which used the "blastwave" delayed cooling model for supernova feedback (Stinson et al. 2006). The simulation successfully produced field dwarf galaxies that follow many observed scaling relations in total stellar and gas mass, metallicity, kinematics, and morphology. The simulated galaxies have extremely bursty SFHs (which cause persistent DM cores (Madau et al. 2014)) and impulsive galactic outflows, resulting in a large metal-enriched CGM. The same group of galaxies was also simulated in Mina et al. (2021) with the more realistic "superbubble" feedback model (Keller et al. 2014) without ad hoc cooling delays to explore the impact of SN feedback models on dwarf galaxy properties (see also Azartash-Namin et al. (2024) for a similar study but with H_2 chemistry and H_2-based star formation). The authors found that while global quantities of galaxies with halo masses of $M_\mathrm{h} > 10^{10}\,\mathrm{M}_\odot$ remain similar with different feedback models, the DM cores, the CGM metals, and the formation of smaller galaxies ($M_\mathrm{h} \sim 10^9\,\mathrm{M}_\odot$ and below) are very sensitive to feedback. In this study, we adopt the exact galaxy formation physics from Mina et al. (2021) but with the addition of RT, which models the transport of radiation from the UVB and the local stellar sources. The use of the same initial condition and resolution provides an ideal setup to be able to compare our approach with previous simulations in order to single out the impact of radiation.

This paper is structured as follows. In Section 2, we briefly present the simulation setup and summarise the main features of the RT implementation and the treatment of the radiation field. In Section 3, we describe the general properties of the simulated dwarf galaxies and analyse the impact of on-the-fly RT on the formation and evolution of dwarf galaxies. We study the properties of the DM halos of the two most massive halos in the simulation, focusing on the cusp-core transformation in Section 4. In Section 5, we explore the CGM of the group of dwarf galaxies and compare it to observational constraints. A summary of our findings is provided in Section 6.

2. Simulation

The simulation has the same initial condition and galaxy formation physics as in Mina et al. (2021) except for the on-the-fly radiative transfer (RT) models. Here, we briefly outline the general setup. The zoom-in simulation was performed using the Tree+Smoothed Particle Hydrodynamics (SPH) code GASOLINE2 (Wadsley et al. 2017), adopting a cosmology with $\Omega_\mathrm{b} = 0.042$, $\Omega_\mathrm{m} = 0.24$, $\Omega_\Lambda = 0.76$, $h = 0.73$ and $\sigma_8 = 0.77$. The simulation box, with a side length of 25 co-moving Mpc (cMpc), hosts a ∼2 cMpc wide high resolution zoom-in region. This zoom region contains about 6 million DM and equally many SPH particles, with a mass resolution of $m_\mathrm{dm} = 1.6 \times 10^4\,\mathrm{M}_\odot$ and $m_\mathrm{SPH} = 3.3 \times 10^3\,\mathrm{M}_\odot$. The gravitational softening length, ε_G, was set to 86 co-moving pc from $z = 129$ to 9 and kept constant at 86 physical pc below $z = 9$. The SPH smoothing length, h, was allowed to shrink to $0.1\,\varepsilon_\mathrm{G}$. The resolution of this simulation is typical for state-of-the-art zoom-in simulations of Milky Way-like galaxies and their satellites (e.g. Wheeler et al. 2019; Applebaum et al. 2021), although recent simulations of field dwarf galaxies have reached higher resolution (e.g. Agertz et al. 2020; Gutcke et al. 2021; Munshi et al. 2021). Since the main objective of this work is to investigate the impact of radiative feedback, we choose to keep the same resolution as in previous works to minimise the uncertainties introduced by resolution. The gas phase composition is initialised as primordial mixture with 76.4% hydrogen and 23.6% helium by mass and zero metallicity. Star formation follows the subgrid model from Stinson et al. (2006), where gas particles probabilistically convert into star particles when gas cools below 10^4 K, reaches a density threshold of $n_{\rm H} \geq 100\,{\rm atoms\,cm^{-3}}$, and is in a convergent flow. The star formation rate follows the Schmidt law (Schmidt 1959):

$$\frac{{\rm d}\rho_\star}{{\rm d}t} = \varepsilon_{\rm SF}\frac{\rho_{\rm gas}}{t_{\rm dyn}} \propto \rho_{\rm gas}^{1.5}, \tag{1}$$

where $\rho_\star$ and $\rho_{\rm gas}$ are the stellar and gas density, respectively, $\varepsilon_{\rm SF} = 0.1$ is the star formation efficiency and $t_{\rm dyn}$ the local dynamical time. The newly formed star particle has an initial mass equal to the parent gas particle, $m_\star = 3.3 \times 10^3\,{\rm M_\odot}$ and each star particle represents a simple stellar population with its stellar mass distribution described by a Kroupa (2001) initial mass function (IMF), population III stars are not explicitly treated. During their lifetimes and at the end of their life, stars return energy, mass, and metals into their surrounding medium. We include feedback from stellar winds, Type Ia and Type II Supernova. These feedback models (both energetic and chemical) remain the same as in Mina et al. (2021). In particular, we use the "superbubble" subgrid model from Keller et al. (2014) for SN II. This model takes into account the development of the superbubble from multiple SNe events, and thermal conduction between the hot and cold phases, which is an important process for cold gas evaporation (e.g. El-Badry et al. 2019).

Following Shen et al. (2014), we track oxygen and iron yields separately using the model from Raiteri et al. (1996).The oxygen and iron abundances are then converted to alpha-element and iron peak-element abundances, respectively, assuming the solar abundance pattern from Asplund et al. (2009). A turbulent diffusion model for metals and thermal energy is also included to account for sub-resolution turbulent mixing processes during gas advection, as described in detail in Shen et al. (2010).

The initial conditions are identical to those used in the simulations of Shen et al. (2014) and Mina et al. (2021). We compare our simulation with RT with both previous simulations, although the main comparison is with the Mina et al. (2021) data since our goal is to understand the dependencies of dwarf galaxy properties on UVB and stellar radiation. In the following, we refer to the simulation analysed in Shen et al. (2014) as Blastwave; the one analysed in Mina et al. (2021) as Superbubble, in accordance with their stellar feedback prescription; and our new run as RT.

2.1. Radiative transfer

On-the-fly radiative transfer is solved using TREVR2 (Wadsley et al. 2024), the new tree-based reverse ray tracing algorithm implemented in GASOLINE2. TREVR2 combines gas particles in tree cells according to the transmission averaging scheme and the rays are built along the direction of HEALPix (Górski et al. 2005) cones. This results in a fast RT algorithm which scales as $O\,(N_{\rm active}\log_2(N))$, where $N_{\rm active}$ is the number of "active particles" (i.e. particles whose properties will be updated in a certain time step), and N is the number of sources.

The source spectra are reconstructed using the piece-wise power-law (PWPL) method described in detail in Baumschlager et al. (2024). In brief, the spectra are represented at nine photon energies located just above and below the ionisation energies of H and He, at 136 and 500 eV and one additional more classical broad Far-UV (FUV) band (5.6–11.2 eV). The placement of the selected photon energies just above and below the ionisation potential of H and He allowed us to accurately track jumps in intensity across the ionisation edges. The method assumes that the spectral shape follows a power-law between these energies.

Table 1. Radiation bands used in the simulation

Band	Photon energy (eV)	Physical effect
FUV	5.6–11.2	
LW-l	11.2^+	
LW-h	13.6^-	
HI-l	13.6^+	H ionisation/heating
HI-h	24.6^-	H ionisation/heating
HeI-l	24.6^+	H & He ionisation/heating
HeI-h	54.4^-	H & He ionisation/heating
HeII-l	54.4^+	H, He & He^+ ionisation/heating
HeII-h	136.0	H, He & He^+ ionisation/heating
XUV	500.0	H, He & He^+ ionisation/heating

Table 1 summarises the selected photon energies and the physical effects they are used for. Furthermore, the photo-ionisation cross-sections for H and He are represented as power-laws, fitted to the photo-ionisation cross-sections from Verner et al. (1996) such that:

$$\sigma_{\rm i,j}(\nu) = \nu^{\beta_{\rm i,j}}\left(S_{\rm i,j} + T_{\rm i,j}\,\nu\right), \tag{2}$$

where $\beta_{\rm i,j}$ is the power-law slope for element i in the radiation band j, i.e. for H in the HeII ionising band (54.4–500.0 eV), and $S_{\rm i,j}$ and $T_{\rm i,j}$ are fitting coefficients, provided in Baumschlager et al. (2024).

2.2. Sources of radiation

The PWPL spectral reconstruction of the radiation field allowed us to combine different sources of radiation, and for the presented simulation, we include both stellar radiation and the UV background. Each stellar particle is treated as a source of radiation, with its intensity and spectral shape defined by its age. The intensity per radiation bin is pre-calculated based on STARBURST99 (Leitherer et al. 2014) spectra. We assume that the stellar population follows a Kroupa (2001) IMF and use the Padova AGB stellar evolution tracks for solar metallicity. We considered population ages between 1 Myr and 13 Gyr for our simulation. For younger and older populations, we assumed the spectral shape and intensity of the 1 Myr and 13 Gyr populations, respectively. The size of the theoretical Strömgren sphere of young stars is 9.8 pc under star formation threshold conditions, which is comparable to the minimal smoothing length of our simulation. The UVB radiation is provided through 128 background sources evenly distributed in a spiral pattern on a sphere at the edge of the simulation box, as described in Grond et al. (2019); Baumschlager et al. (2024). These background sources follow the redshift dependent background spectrum of Haardt & Madau (2012) from $z \sim 15.2$ to 0. Rather than instantly switching on the UVB, we increase the intensity between redshift 16 and 15.2 from zero intensity to the Haardt & Madau (2012) intensity.

2.3. Chemical network coupled with RT

The simulation includes radiative cooling and heating over a temperature range $T = 10\text{–}10^9$ K. The narrow band approximation and the power-law fits to the photo-ionisation cross section allowed us to analytically approximate the photo-ionisation and photo-heating rates for arbitrary shapes of radiation source spectra with great accuracy (cf. Equation (8) and (9) in

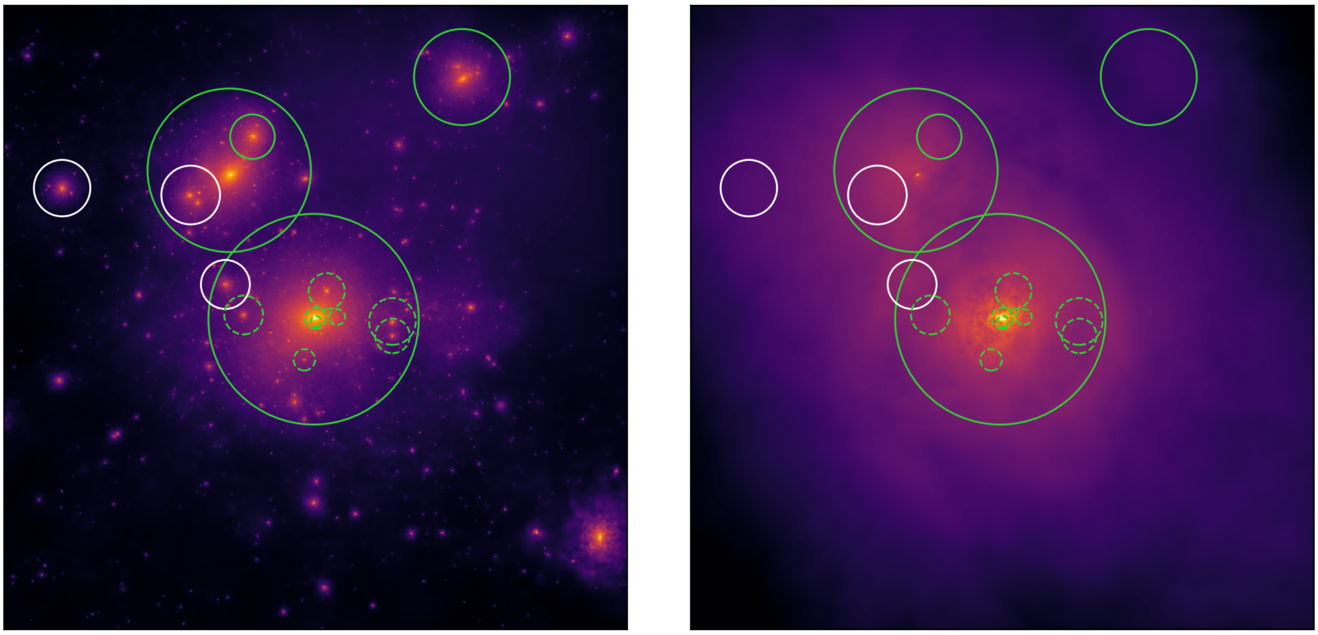

Fig. 1. Projected DM (left) and gas (right) density in a cube of 500 kpc per side at $z = 0$, centred on Bashful, the most massive halo in the simulation volume. The circles mark the viral radii of the identified galaxies, where the solid circles indicate the positions of the original seven dwarfs and dashed lines highlight the locations of the quenched satellite galaxies of Bashful. Green lines indicate halos that formed stars at some point during the simulation.

Baumschlager et al. 2024). Thus, the abundances, heating and cooling rates of the primordial species (H, H+, He, He+ and He++) are computed with the non-equilibrium chemical network (Shen et al. 2010), with photoionisation rates calculated from both the UV background (Haardt & Madau 2012) and local stellar radiation. Chemistry of molecular hydrogen (H_2) is not followed in this simulation for simplicity. However, we note that H_2 formation and disassociation can play an important role in dwarf galaxies (e.g. Munshi et al. 2019). The current implementation of H_2 in GASOLINE2 and CHANGA is based on a local estimation of the Lyman-Werner radiation (Christensen et al. 2012), and we plan to couple the solver fully with RT in an upcoming paper. For this work, it is informative to isolate and understand the impact of ionising radiation without involving the complexity of H_2-based star formation.

For metal-line cooling and heating, we continue to use the rates from CLOUDY (Ferland et al. 2017) assuming photoionisation equilibrium under a uniform UVB. We note that this approach is not entirely consistent, as the ionisation abundances of metals are dependent on the local radiation field in the ISM and the CGM. However, including a metal chemical network or tabulated cooling rates with a non-uniform, multi-frequency radiation field is computationally or memory expensive for cosmological simulations evolving to $z = 0$. Therefore, we have adopted this simpler model for metal cooling and defer a more detailed study to future work.

3. Properties of the simulated galaxies

We illustrate the selected zoom-region in Fig. 1, where we show the projected DM density (left) and gas surface density (right) in a $(500\,\mathrm{kpc})^3$ box centred on "Bashful", the most massive halo in the volume, at redshift zero. The solid circles indicate the locations and sizes of the seven most massive halos with non-zero gas content, with their radii corresponding to the virial radii. These galaxies are the same as the ones investigated in Mina et al. (2021) and Shen et al. (2014). The four halos with star formation (Bashful, Doc, Dopey and Grumpy) are indicated with green lines, and the three starless halos are indicated with white lines. All galaxies are "field" dwarf galaxies, as the closest massive halo ($M_{\rm vir} = 2.5 \times 10^{12}\,\mathrm{M}_\odot$) is located more than 3 Mpc away. Nevertheless, these galaxies themselves are interacting towards $z = 0$, as shown clearly by the location of the circles. In addition, the simulation contains eight new satellite galaxies that appear to be completely quenched, which are labelled with the dashed circles.

The global properties of the dwarf galaxies are shown in Table 2. The seven named galaxies refer to the same halos as in Shen et al. (2014) and Mina et al. (2021), and those labelled as *qDG* refer to the population of quenched satellite galaxies of Bashful, which did not form stars in the previous runs. These galaxies have typical stellar mass around 10^4 to 10^5 solar masses, but only contain very old stellar populations, which suggests that they are relics from reionisation. We discuss them in detail in Section 3.3. In general, we found that the impact of radiation on galaxy properties strongly depends on the halo mass. Thus, we present the results for the two most luminous galaxies ($M_{\rm vir} > 10^{10}\,\mathrm{M}_\odot$) first, followed by the fainter galaxies with $M_{\rm vir} \sim 10^9 - 10^{10}\,\mathrm{M}_\odot$, and finally, we discuss the faintest population.

3.1. Two Luminous Dwarfs

The stellar mass–halo mass (SMHM) relation and the SFH of the simulated galaxies are shown in Figure 2. The present day stellar mass ($M_\star$) of the two most massive dwarf galaxies with $M_{\rm vir} > 10^{10}\,\mathrm{M}_\odot$, Bashful and Doc, are $5.0 \times 10^7\,\mathrm{M}_\odot$ and $1.0 \times 10^7\,\mathrm{M}_\odot$, which correspond to a stellar mass fraction of 0.0014 and 6.2×10^{-4}, respectively. These are in excellent agreement with the observational data of isolated and satellite dwarf galaxies from the Local Group

Table 2. Properties of the simulated dwarf galaxies at redshift zero.

Name	M_{vir} ($M_\odot$)	R_{vir} (kpc)	V_{max} (km s^{-1})	$M_\star$ ($M_\odot$)	M_{gas} ($M_\odot$)	M_{HI} ($M_\odot$)	f_b	⟨[Fe/H]⟩	M_V	$B-V$
Bashful	3.47×10^{10}	84.43	48.13	4.96×10^{7}	9.79×10^{8}	3.49×10^{7}	0.030	-1.40 ± 0.94	−14.54	0.54
Doc	1.62×10^{10}	65.54	36.98	1.01×10^{7}	2.67×10^{8}	6.74×10^{5}	0.017	-1.64 ± 1.27	−12.28	0.67
Dopey	3.29×10^{9}	38.51	22.42	2.95×10^{5}	2.04×10^{7}	3.79×10^{2}	0.006	-2.83 ± 1.24	−8.32	0.69
Grumpy	1.77×10^{9}	17.88	21.77	7.51×10^{5}	6.37×10^{6}	2.02×10^{2}	0.004	-2.74 ± 1.24	−9.38	0.70
Happy	7.51×10^{8}	23.54	15.54	–	8.67×10^{5}	3.39×10^{1}	0.001	–	–	–
Sleepy	4.36×10^{8}	19.63	13.71	–	–	–	–	–	–	–
Sneezy	6.68×10^{8}	22.63	14.90	–	2.79×10^{6}	7.35×10^{1}	0.004	–	–	–
qDG1	3.81×10^{8}	18.77	13.37	1.71×10^{5}	9.80×10^{6}	3.63×10^{2}	0.026	-3.14 ± 0.70	−7.77	0.70
qDG2	2.42×10^{8}	14.47	16.04	6.33×10^{5}	4.45×10^{4}	4.69×10^{0}	0.003	-2.37 ± 0.78	−9.15	0.69
qDG3	2.17×10^{8}	15.56	13.07	7.90×10^{5}	1.45×10^{6}	4.66×10^{1}	0.010	-2.36 ± 1.33	−9.42	0.70
qDG4	1.54×10^{8}	13.88	11.60	1.18×10^{5}	–	–	0.001	-2.58 ± 0.92	−7.32	0.69
qDG5	3.55×10^{7}	8.52	9.34	1.14×10^{5}	–	–	0.003	-3.28 ± 0.60	−7.37	0.71
qDG6	3.55×10^{7}	8.58	8.31	8.26×10^{4}	–	–	0.002	-3.23 ± 0.45	−6.99	0.70
qDG7	4.99×10^{6}	6.32	3.64	7.43×10^{4}	–	–	0.015	-2.82 ± 0.95	−6.84	0.69
qDG8	2.10×10^{6}	4.23	3.40	2.48×10^{4}	–	–	0.012	-2.66 ± 1.03	−5.61	0.69

Notes. Column 1 lists the name of the dwarf galaxy. Columns 2–11 provide the present-day viral mass, viral radius, maximum circular velocity, stellar mass, gas mass, HI mass, baryon fraction $f_b = (M_\star + M_{gas})/M_{vir}$, mean stellar metallicity, V-band magnitudes and $B-V$ colour.

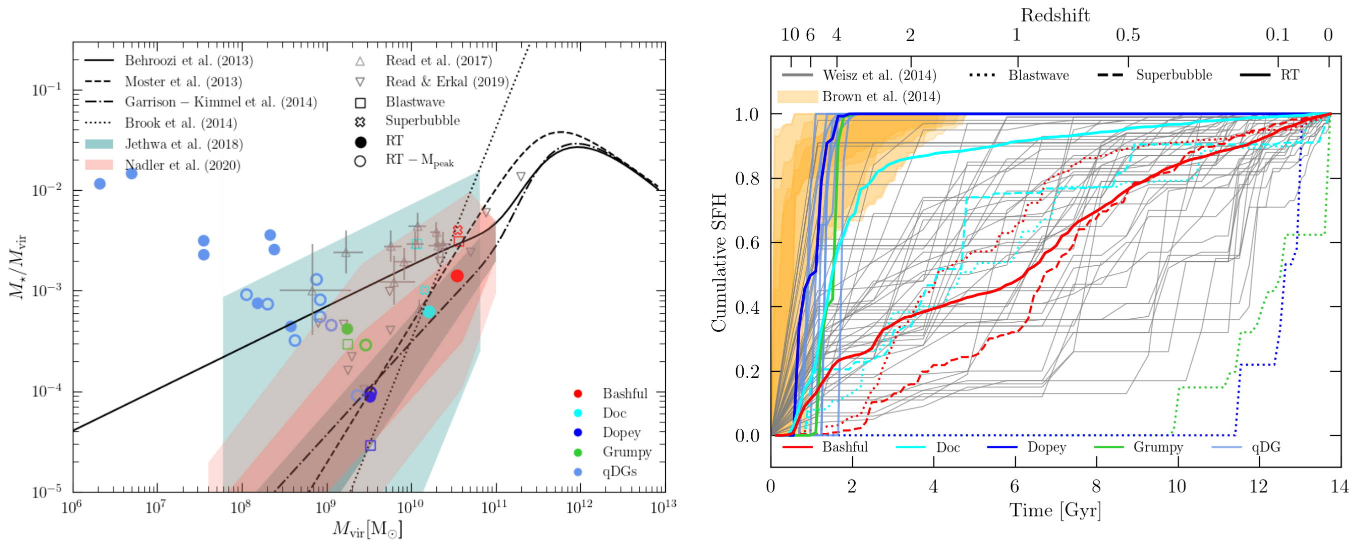

Fig. 2. *Left panel*: stellar mass–halo mass relation. The circles show the results of this work. The filled circles show the stellar fraction as a function of halo mass at $z = 0$, and the open ones show results at the redshift where the halo mass is at its peak value (i.e. before tidal stripping during the accretion process). For comparison, the open crosses show the Superbubble run from Mina et al. (2021), and the squares indicate the Blastwave run from Shen et al. (2014). Open gray triangles represent the sample of isolated dwarf galaxies from Read et al. (2017) and satellite galaxies from Read & Erkal (2019). The black lines show the mean present-day SMHM relation of Behroozi et al. (2013) (solid), Moster et al. (2013) (dashed), Garrison-Kimmel et al. (2014) (dot-dashed) and Brook et al. (2014) (dotted). The blue and pink contours indicate SMHM relations from Jethwa et al. (2018) and Nadler et al. (2020), respectively. The darker contour corresponds to 1σ scatter and the lighter one indicates 2σ scatter. *Right panel*: cumulative SFH of the simulated dwarf galaxies. Coloured lines represent the galaxies formed in the simulations. Solid lines show the results of the RT run, colour-coded as indicated in the Figure. Dotted and dashed lines correspond to the Blastwave and Superbubble runs, respectively. Grey lines show the SFH derived from Weisz et al. (2014) for Local Group dwarfs and orange shaded regions show the SFH of UFDs from Brown et al. (2014).

(Read et al. 2017; Read & Erkal 2019) and the extrapolation of SMHM relations from abundance matching (AM) technique (Moster et al. 2013; Brook et al. 2014; Garrison-Kimmel et al. 2014; Jethwa et al. 2018; Nadler et al. 2020) although somewhat below the AM relation derived by Behroozi et al. (2013). The comparison between this work (filled circles) and the run with superbubble feedback only (open crosses) from Mina et al. (2021) indicates that the radiative feedback suppresses star formation by a factor of 2–3 in this classical dwarf galaxy regime.

The cumulative SFH shows that both Bashful and Doc are star-forming at $z = 0$. Comparing the RT simulation results (solid line) with superbubble feedback only (dashed line), we find that

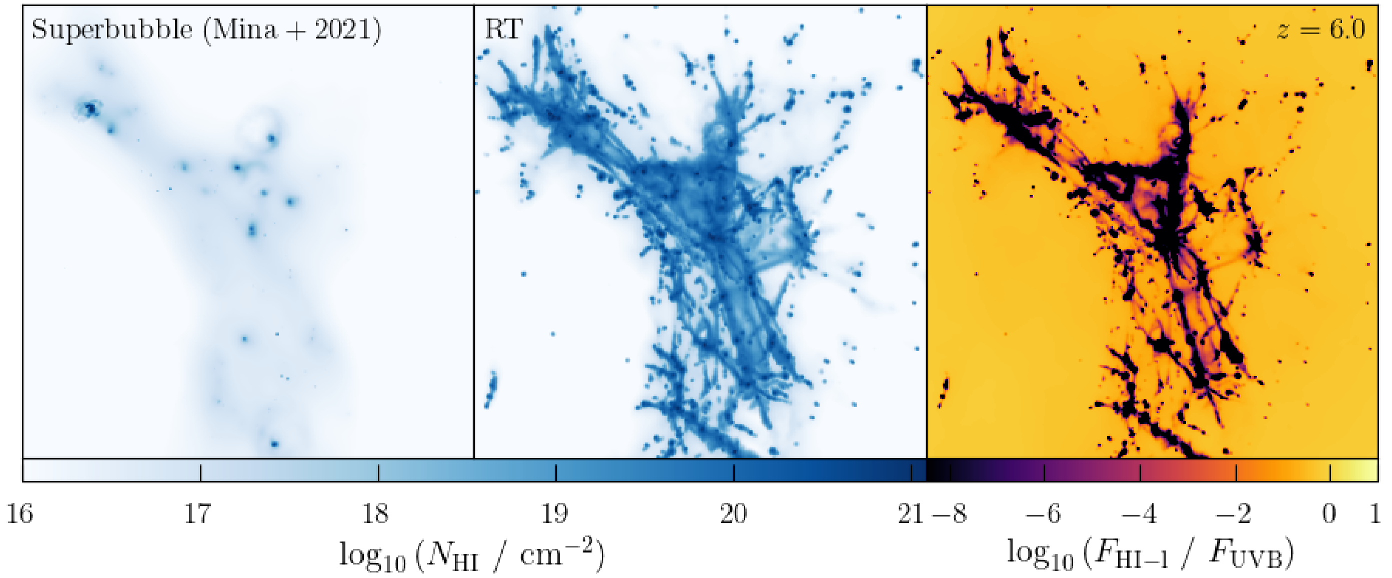

Fig. 3. Projected HI density ($N_{\rm HI}$) in a cube with one cMpc per side at $z = 6$ for the Superbubble (left) and RT (middle) run. Right: density weighted radiation field relative to the Haardt & Madau (2012) UVB flux in the HI-1 band at 13.6 eV.

the inclusion of RT increases the fraction of old stellar populations. In particular, Doc has more than 80% of stars formed at $z \geq 3$. This is mostly due to the increase in early star formation before and during reionisation. Unlike the typical approach of turning on the uniform UV background instantaneously as used in Shen et al. (2014) and Mina et al. (2021), with RT, the UV background radiation is emitted from virtual background sources, distributed close to the edge of the simulation box. As the ionisation front associated with the UVB has to propagate through the IGM, it does not reach the halos immediately. This time delay[1] prevents gas from heating up and allows it to cool and collapse to higher densities, enabling the galaxies to form stars during the EoR. This effect is demonstrated in Figure 3. The left and middle panels show the neutral hydrogen column density $N_{\rm HI}$ at $z = 6.0$ from the Mina et al. (2021) superbubble simulation, and our simulation with RT, respectively. With RT there is significantly more HI gas at this redshift, especially in the halos and the filaments connecting them where the radiation has not yet penetrated through. This is shown in the right panel of Figure 3. The flux of ionising radiation within halos and filaments is much smaller than the UV background value. Focusing back on the SFH properties in Figure 2, we find that the impact of radiation on the SFH is dependent on galaxy halo mass, with lower mass halos (Doc) being more sensitive to radiation and photo-heating than higher mass halos (Bashful), and this effect is even more obvious for the smallest mass halos (cf. Section 3.2).

3.2. Two fainter dwarfs

Dopey and Grumpy are the two fainter galaxies with halo mass $M_{\rm vir} \sim 10^9$–10^{10} M$_\odot$ and stellar mass fraction of 9.0×10^{-5} and 4.2×10^{-4}, respectively. Although this is again in agreement with the abundance matching results, it is interesting that these two galaxies do not form in the SN feedback-only simulation with the superbubble model (Mina et al. 2021). As shown in the right panel of Figure 2, in the RT simulation the stellar population is old, with the majority of star formation occurring before $z \sim 4$. More precisely, Dopey and Grumpy start forming their stars during the era of reionisation ($z = 8.52$ and 5.5 respectively) and cease SF by $z = 3.47$ and 3.27, respectively. Such an SFH is very similar to the observed UFDs in the Local Group (e.g. Brown et al. 2014), although Dopey and Grumpy have somewhat higher masses than typical UFDs ($M_{\rm v} > -7.0$, Simon 2019). The early star formation is again related to the propagation of the UVB in the RT simulation, which allows the IGM to be mostly neutral and cold for a longer time so that it can accrete onto small halos such as the progenitors of Dopey and Grumpy. No star formation occurred at lower redshift when the reionisation was complete, which is consistent with the Superbubble run results. Nevertheless, the same halos form galaxies in the Blastwave run in Shen et al. (2014) with completely opposite SFHs (dotted lines in the right panel of Figure 2). They have similar mass but predominantly young stellar populations. Our results highlight how sensitive the formation of the faintest dwarf galaxies depends on reionisation history, radiative feedback, SN feedback models, and the chemical and thermodynamic states of the circumgalactic gas.

3.3. The quenched satellites

Comparing to the Blastwave and the Superbubble runs, we find eight more quenched dwarf galaxies (qDGs) in the simulation volume, all of which are satellites of Bashful at $z = 0$. These galaxies have halo masses ranging from 10^6 M$_\odot$ to a few times 10^8 M$_\odot$ at $z = 0$, but with typical stellar mass $\sim 10^4$–10^6 M$_\odot$. The three smallest galaxies qDG6, qDG7 and qDG8 have $M_{\rm v} > -7.0$ and can be classified as UFDs. The smallest halos have stellar mass fractions much higher than the extrapolation of the stellar mass-halo mass relations. However, as shown in Table 3, the halo masses before accretion ($M_{\rm peak}$) are significantly larger, ranging from 10^8 to a few times 10^9 M$_\odot$, indicating strong tidal stripping of DM during the accretion process. The ratios between current and peak halo mass for these halos are less than 40% and can be as low as 0.25–0.44% (qDG8 and qDG7, respectively). The

[1] We note that this time delay is due to the R-type expansion of the ionisation front, rather than the speed of light. TREVR2 assumes infinite speed of light as it is an instantaneous method.

Table 3. Bashful's quiescent satellite population.

Name	$z_{\rm SF,first}$	$z_{\rm SF,last}$	$\Delta t_{\rm SF}$ (Myr)	$z_{\rm infall}$	$M_{\rm HI,infall}$ ($M_\odot$)	$M_{\rm peak}$ ($M_\odot$)	$M_{\rm vir}/M_{\rm peak}$	σ (km/s)
qDG1	4.857	4.141	275.5	0.59	135.1	2.32×10^{9}	0.16	8.67
qDG2	8.098	3.172	1460.3	1.70	86.6	8.47×10^{8}	0.29	7.64
qDG3	5.469	3.985	525.0	1.39	127.6	7.65×10^{8}	0.28	6.56
qDG4	7.030	4.165	746.9	1.18	15.3	4.26×10^{8}	0.36	7.78
qDG5	3.881	3.575	170.0	2.43	97.9	2.03×10^{8}	0.17	6.41
qDG6	4.784	3.806	415.3	1.75	0.89	1.14×10^{8}	0.31	5.79
qDG7	5.992	4.596	388.5	2.66	2.7×10^{3}	1.14×10^{9}	0.0044	2.73
qDG8	6.953	5.833	206.8	3.35	3.8×10^{3}	8.45×10^{8}	0.0025	2.00

Notes. Column 1 lists the name of the dwarf galaxy. Columns 2 and 3 are the redshift of the first and last star formation event. Column 4 gives the time interval from the first to last star formation event in Myr. Columns 5 and 6 are the redshift when the halo approaches $2\times R_{\rm vir}$ of Bashful and the HI mass at this redshift. Columns 7 and 8 are the peak halo mass and the ratio of the present day virial mass to peak halo mass. Column 9 lists the line-of-sight velocity dispersion.

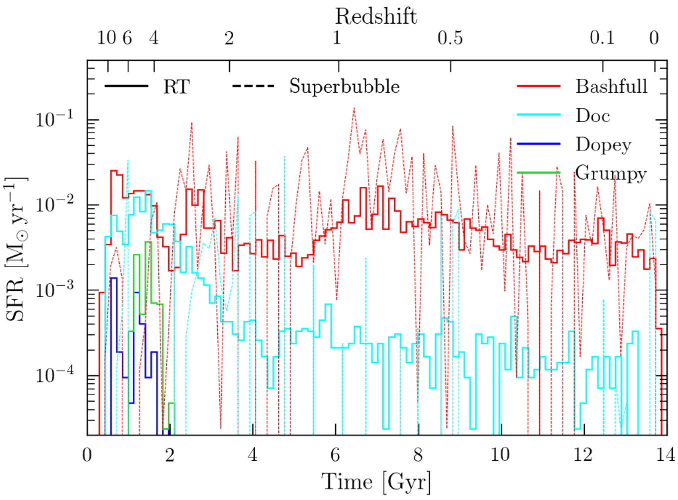

Fig. 4. Star formation rates of Bashful, Doc, Dopey and Grumpy as a function of time and redshift. The thin, dashed lines with similar colours indicate the results from the Mina et al. (2021) run which is without RT but with the same superbubble feedback.

stellar mass fraction as a function of $M_{\rm vir,peak}$ is fully consistent with the SMHM relations from Behroozi et al. (2013) and Jethwa et al. (2018) and observations of isolated galaxies from Read et al. (2017). Similar to Dopey and Grumpy, the qDGs contain only old stellar populations, are red in B-V colours, and are in agreement with the SFHs of observed UFDs. It is worth noting that the halos "Happy", "Sleepy", and "Sneezy" all have masses above 10^8 $M_\odot$, which is similar to or higher than the peak halo mass of some qDGs, and yet there is no early star formation.

3.4. Star formation rate

In Figure 4, we show the star formation rates of Bashful, Doc, Dopey and Grumpy. The Superbubble run from Mina et al. (2021) is also plotted for comparison (where only the two most massive halos form galaxies). When RT is included, although the SFHs are still bursty with rapid changes of the SFR, the amplitude of the changes is generally much smaller than the ones in the Superbubble run. It is likely that radiative feedback and photoheating precondition the ISM, such that the star formation occurs in smaller clumps, which results in weaker collective SN feedback and galactic outflows and hence less suppression of star formation. In the RT run SF within Bashful is typically distributed over the central 1.5 kpc and star particles are formed in isolation or in small groups of less than five particles ($\lesssim 1.6\times10^4$ $M_\odot$) within 100 pc. In the Superbubble run SF occurs in distinct bursts with durations of approximately 50–100 Myr during which a few massive clusters of stars are formed. These often contain hundreds of star particles (with mass $\sim10^5$–10^6 $M_\odot$) within several hundred parsec and are able to form at distances of up to 4 kpc from the centre.

Our results are consistent with previous RT simulations of idealised disc galaxies (e.g. Rosdahl et al. 2015) with similar resolution. It also agrees with Smith et al. (2021) in their idealised simulations with a much higher resolution (20 $M_\odot$), where ionising radiation leads to a more compact stellar disc and less clustered SNe. Interestingly, they argue that a high resolution is required to capture the full impact of photoionisation because at a lower resolution, one star particle of 1000 $M_\odot$ alone can produce more than 10 SNe, which is already a greater number of SN than their typical SN clustering. In our simulation, however, the star cluster mass without radiative feedback is typically much higher, especially at high redshift. It is likely that rapid gas accretion and frequent mergers at high redshift result in starbursts in more massive clusters, which differs significantly from well-settled, isolated disc setups. Bursty star formation caused by disruptive outflows is often associated with the DM cores, as these outflows often result in a rapid change of the central gravitational potential wells (e.g. Governato et al. 2010; Pontzen & Governato 2012). As radiative feedback renders the star formation less bursty, it is expected that the formation of the DM core is also impacted. We discuss this in detail in Section 4.

As star formation is suppressed less strongly by SNe, the SFH in both Bashful and Doc lacks an extended quiescent period, during which SF is completely quenched. This is different from the Superbubble simulation, especially for the lower mass Doc. Observationally, resolved stellar population analysis for the Local Group dwarf galaxies does show breaks of star formation activity for tens to hundreds of million years or longer in some galaxies (Tolstoy et al. 2009), which may indicate the collective effect of feedback in these systems is stronger than in our simulation. However, the observed SFHs are still highly diverse among different galaxies and long quenched periods are not common (e.g. McQuinn et al. 2024). In general, a quiescent period does not necessarily imply that feedback is more "ejective". Preventive processes such as photoionisation heating can quench dwarf galaxies (as it does for Dopey, Grumpy, and all

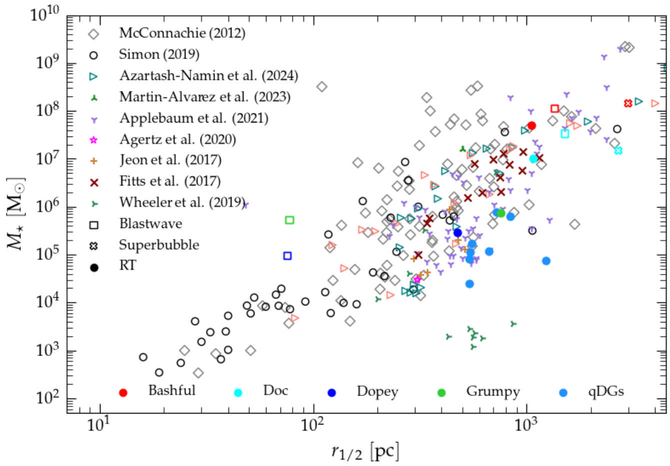

Fig. 5. Stellar mass versus half-light radius of the simulated dwarf galaxies, compared to observations from McConnachie (2012) and Simon (2019); simulations form Jeon et al. (2017); Fitts et al. (2017); Wheeler et al. (2019); Applebaum et al. (2021); Azartash-Namin et al. (2024); and RT simulations from Agertz et al. (2020) and Martin-Alvarez et al. (2023). For the Azartash-Namin et al. (2024) data points, the teal and light red colours correspond to their Blastwave and Superbubble run, respectively.

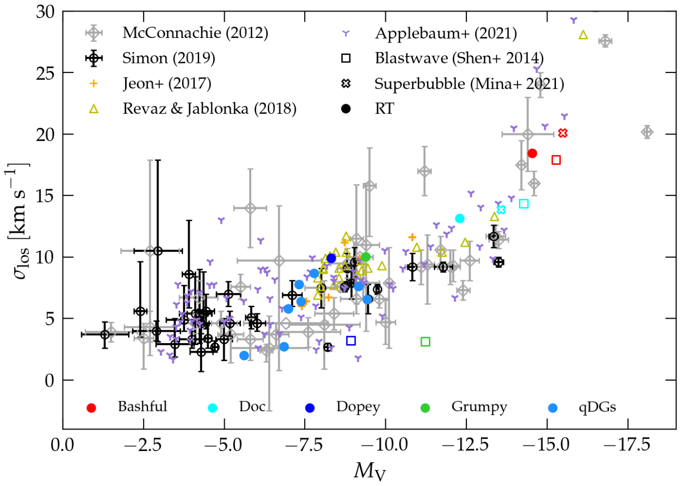

Fig. 6. Luminosity-velocity dispersion ($M_{\rm V} - \sigma_{\rm los}$) relation of the simulated dwarf galaxies compared to observations from McConnachie (2012) and Simon (2019) and simulations from Jeon et al. (2017), Revaz & Jablonka (2018) and Applebaum et al. (2021). Solid circles show the results of the new RT run, colour-coded as indicated; open squares and crosses correspond to the Blastwave and Superbubble runs.

the qDGs in our simulation). In addition, environmental factors such as mergers and ram-pressure stripping cannot be neglected for satellite dwarfs. As our simulation sample is small, it is not sufficient to address the diversity of SFHs in various mass halos and environments. Theoretically, many other simulations also demonstrate a strong burstiness of their SFH and long quiescent times (e.g. Macciò et al. 2017; Fitts et al. 2017; Wright et al. 2019; Applebaum et al. 2021), but again, there is no clear observational evidence that observed dwarf galaxies should be as bursty (Governato et al. 2015). It is recently shown by Zhang et al. (2024) that such burstiness is sensitive to the implementations of SN feedback, in particular the directions of the momentum injection. Our result further indicates that the SFH is sensitive to the interplay between radiation and SN feedback.

3.5. Stellar distribution and kinematics

In Figure 5, we compare the stellar half-light radius, $r_{1/2}$, of our simulated galaxies to the previous seven dwarfs simulations, various simulations from other groups, and also observations from McConnachie (2012) and Simon (2019). For simplicity and comparison with other simulations, our $r_{1/2}$ is the circular half-light radius which is directly computed from the simulation data by summing up luminosity from each stellar particle from the centre until half of the total luminosity is reached. We note that this gives slightly different results from the observationally estimated $r_{1/2}$.The simulated galaxies in this work (solid dots) have $r_{1/2}$ between 476 pc and about 1.2 kpc, which are generally consistent with observations and other simulation works. Comparing to the Superbubble run (empty crosses in the figure), we note that the inclusion of radiation reduces the stellar half-light radius significantly for Bashful and Doc, by about a factor of 2–3, which makes it more consistent with observations. This is an interesting result, and again indicates that feedback-driven outflows are weaker with RT. Early galaxy formation simulations with ineffective feedback often result in compact, bulgy galaxies (e.g. Scannapieco et al. 2012), which is known as the "angular momentum catastrophe". Galactic outflows are shown to eject lower angular momentum gas and thus enable disc galaxies to form (e.g. Brook et al. 2011). Moreover, Mina et al. (2021) compared the superbubble feedback with the delayed-cooling blastwave feedback (shown also here in Figure 5 in open squares), and concluded that the superbubble model drives stronger outflows with higher mass-loading factor than in the delayed-cooling model, and thus creates more extended stellar discs. However, it is worth noting that the behaviour of a feedback model depends on star formation models and total energy input. In Azartash-Namin et al. (2024), the authors compared the superbubble and blastwave feedback models (triangle symbols with light red and teal colours, respectively) in the Storm simulations, but found no clear difference in galaxy sizes between the two. It is likely because the Storm simulation uses an H_2-based star formation model which alters the burstyness of star formation, and a higher energy input per SNe than the Blastwave run. In the current work, the reduction of $r_{1/2}$ clearly suggests that outflows are less strong with RT, possibly as a result of less-clustered star formation, as discussed in Section 3.4.

As expected, the smaller galaxies Dopey, Grumpy, and the qDGs usually have smaller sizes than Bashful and Doc. It is worth noting that the drastically different SFHs in Dopey and Grumpy between our simulation and the ones in Shen et al. (2014) also lead to different galaxy sizes. Dopey and Grumpy in Shen et al. (2014) are blue and very compact, with half-light radii only 80–90 pc (dark blue and green open squares), whereas in our simulation they are much more extended ($r_{1/2}$ about 476 pc and 759 pc for Dopey and Grumpy, respectively). Shen et al. (2014) found that these two galaxies have formation histories and morphologies similar to extremely metal-deficient blue compact dwarfs (XBCD; Papaderos et al. 2008), and argued that the compactness is due to the dynamically unsettled stellar population. In our simulation, these two dwarfs are similar to normal UFDs with only an ancient stellar population, and in this case they reach dynamical equilibrium with the gravitational potential wells.

In Figure 6, we show the relation between the V-band magnitude and the 1D line-of-sight velocity dispersion. The simulated galaxies have a $M_v - \sigma_{los}$ relation in good agreement with observations of Local Group dwarfs from McConnachie (2012) and UFDs from Simon (2019): the velocity dispersion decreases with decreasing luminosity (mass) and plateaus at $M_v \gtrsim -10$, although the scatter is high towards the faint end. Comparing with the Superbubble (open crosses) and Blastwave (open squares) simulations, we find that the inclusion of RT or varying feedback implementations does not strongly affect the stellar velocity dispersion for Bashful and Doc, which indicates that stellar kinematics are less sensitive to radiative and mechanical feedback in the ISM. Similar conclusions are also reached in Agertz et al. (2020) with the EDGE dwarf simulations with various resolutions, feedback, and also RT. Nevertheless, for Dopey and Grumpy, our simulation produced a much higher velocity dispersion than that of the Blastwave run, possibly also due to the fact that the SFH is drastically different between the two simulations, and the galaxies in the Blastwave run have entirely young stellar populations and thus are not dynamically settled.

Although internal processes such as feedback and RT may not strongly impact stellar kinematics, dynamical interactions and tidal stripping are likely to play an important role. All our quenched satellites (qDGs) have smaller velocity dispersion compared to the field dwarfs, even for the ones with similar or higher stellar mass (e.g. qDG2, qDG3 compared to Dopey and Grumpy see Table 2). As noted in Section 3.3, these halos experience severe tidal stripping when they accrete onto Bashful. As demonstrated most recently in Applebaum et al. (2021) with the Justice League simulation of dwarf satellites in the Local Group, σ_{los} of satellite galaxies appear to be proportional to $M_{vir,z=0}/M_{peak}$ (which indicates the severity of stripping), and in their simulations, the majority of galaxies with low velocity dispersion ($\sigma < 5$ km/s) are stripped when accreting onto the Milky Way. Our simulation confirms this result. In fact, the only two galaxies with $\sigma < 5$ km/s in our sample are qDG7 and qDG8, which have the strongest stripping and the smallest M_{vir} at $z = 0$ (cf. Table 3). Tidal interactions reduce stellar velocity dispersion, even though the host halo (Bashful) is small compared to the MW-mass halos in Applebaum et al. (2021).

3.6. Metallicities

The MZR or luminosity-metallicity relation (LZR) is one of the fundamental scaling relations observed in galaxies across many orders of magnitude in mass. For dwarf galaxies in the Local Group (both dSphs and dIrrs), it has been shown from resolved stellar population studies that they follow a universal MZR(LZR) despite having different photometries and morphologies (e.g. Kirby et al. 2011, 2013). Dwarf galaxies are typically metal-poor, and chemical evolution models suggest that a large fraction (if not the majority) of metals are ejected from galaxies. The MZR extends well into the UFD mass regime, although the metallicities appear to plateau around [Fe/H] ~ -3.0 at the faintest end, and the relation has significantly larger scatter (Simon 2019). Figure 7 shows the stellar LZR compared to the observations of the Local Group satellite and irregular dwarf galaxies (McConnachie 2012; Kirby et al. 2013) and the UFDs of Simon (2019) and Fu et al. (2023). When computing the average metallicity, here we do not add a metallicity floor of [Fe/H]=–4.0, as has been done in some previous work (e.g. Fitts et al. 2017; Applebaum et al. 2021) to account for the early enrichment from Population III stars. But in practice, adding such a floor does not impact our results.

Similarly to previous seven dwarfs simulations, the metallicities of Bashful and Doc are fully consistent with the observed

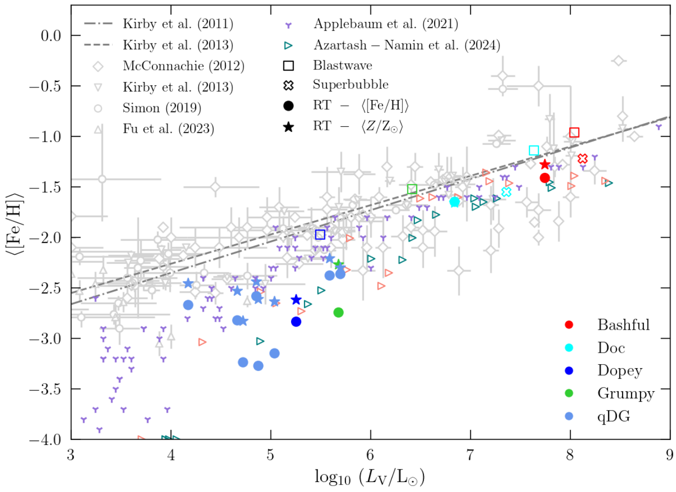

Fig. 7. Stellar luminosity-metallicity relation of the simulated dwarf galaxies. The solid circles show the results of this work, and the coloured crosses and squares indicate the previous seven dwarfs simulation of Mina et al. (2021) (superbubble feedback, no RT) and Shen et al. (2014) (blastwave feedback, no RT), respectively. The grey symbols represent observations of Milky Way and Andromeda satellite galaxies (McConnachie 2012; Kirby et al. 2013); open black circles and open stars show observations of local UFDs from Simon (2019) and Fu et al. (2023). The gray lines show the best fit to the LZR of the Milky Way dwarf satellite galaxies (Kirby et al. 2011) and of Local Group dwarf galaxies (Kirby et al. 2013). For comparison, we also plot simulation data from Applebaum et al. (2021) (purple symbols) and Azartash-Namin et al. (2024) (teal and light red triangles for their Blastwave and Superbubble simulations, respectively).

MZR. Compared to the Superbubble run (cross symbols), our RT simulation decreases the average stellar metallicity proportionally to the decrement in stellar mass, such that the data points still have a similar slope as the Kirby et al. (2011) fitting function. This is particularly interesting for Doc, as it has a much older stellar population than the previous Superbubble simulations (cf. Figure 2, right panel), and yet the metallicity does not decrease significantly, which suggests that the high-z ISM of Doc retains more metals. For example, at $z = 4$ Doc's ISM retained approximately 10% of the produced metals in the RT run while this number is only 5% in the Superbubble run.

For fainter galaxies with $L < 10^6\,L_\odot$, the average metallicity is systematically lower than the observations, especially for the satellites qDG1, qDG5, qDG6 (which have <[Fe/H] >< −3.0) and the dIrrs Dopey and Grumpy. To understand this, we show the metallicity distribution function (MDF) for all faint galaxies in our simulation in Figure 8. We compare with recent observations of 13 MW UFDs from HST narrowband imaging by Fu et al. (2023). Following the procedure in Fu et al. (2023), we exclude stellar particles with [Fe/H]< –4.8. Note that some galaxies in our sample have slightly higher stellar mass, so they are not strictly UFDs, but such a comparison can still be illustrative. In general, the simulation overproduces the number of low-metallicity stars with [Fe/H] < -3.0, while lacking stars with higher metallicities. The peak of the MDF is around [Fe/H] ~ -3.5 in our simulated faint galaxies, but around –2.5 for observed UFDs. The fraction of stellar particles with [Fe/H] < -3.0 for qDG1, qDG5 is qDG6 88%, 85% and 89%, respectively. It is therefore unsurprising that the average metallicities are below the observed MZR for these galaxies. Several factors can contribute to this. First, feedback processes may eject

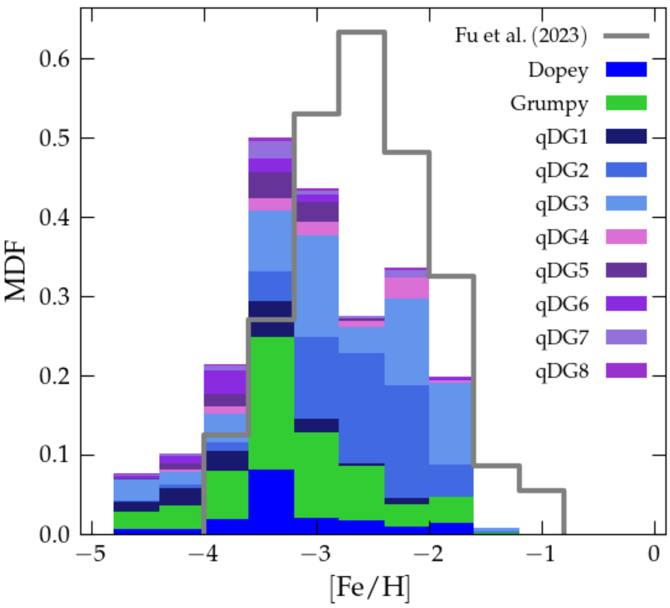

Fig. 8. The metallicity distribution function for Dopey, Grumpy and all qDGs (all galaxies with $L_v < 10^6$ L$_\odot$). To compare with the UFD observations from Fu et al. (2023), we have removed stellar particles with [Fe/H] < −4.8 from the sample. The composite MDF of 13 Milky Way UFDs from Fu et al. (2023) is plotted with a gray line.

too much metal from the ISM. For example, Agertz et al. (2020) showed that boosting SN feedback energy significantly decreases [Fe/H] in the EDGE simulations. It was argued that MZR or LZR is a critical test to differentiate galaxy formation models in simulations. Although ejective feedback is possibly the most important factor in reproducing the MZR, a second factor is the relative abundances of different elements. For stellar LZR, iron abundances are most often measured to represent metallicities. However, iron yields are still highly uncertain, especially from Type Ia supernovae. More recent stellar evolution and yield models for SN II (e.g. Pignatari et al. 2016) and SN Ia (e.g. Leung & Nomoto 2018) significantly boost Fe production at an early time (e.g. Hopkins et al. 2023). In Figure 7, we show the actual average metallicity ($Z/Z_\odot$) of the simulated galaxies (star symbols). Here, the simulation appears to be more consistent with the observations, especially at the fainter end. It is possible that our yield models adopted from Raiteri et al. (1996) underestimate iron abundances, as they are older models. Similar results are also found in the Justice League simulation in Applebaum et al. (2021), which uses the same yield models as in our work. We defer to future work to investigate the role of chemical enrichment models in the MZRs. One of the strong, but complementary constraints to understand the MZR is the metal content in the circumgalactic and the intergalactic media, but CGM and IGM observations are not without challenges, especially for faint, satellite dwarf galaxies, where their CGM is often shared with the more massive host. We discuss the CGM from our simulation in Section 5.

In Figure 7, we also show data from the Justice League simulation from Applebaum et al. (2021) and the Storm simulation from Azartash-Namin et al. (2024) for comparison, since the three simulations use similar hydrodynamic codes, metal diffusion, and yield models. The main differences are that both Applebaum et al. (2021) and Azartash-Namin et al. (2024) use an H_2-based star formation model and they do not have RT. The Justice League simulation uses the blastwave feedback model of Stinson et al. (2006) and simulates Local Group analogues, whereas the Storm suite uses both the blastwave and the superbubble feedback models and simulates more isolated dwarf systems (although the most massive halo is still larger than our simulation, with $M_{vir} \sim 10^{11}$ M$_\odot$). It is interesting that the faint galaxies within $L_V \sim 10^4$–10^6 L$_\odot$ in Applebaum et al. (2021) generally have higher metallicities than our simulation and are more consistent with observations (although still at the lower end), but the Azartash-Namin et al. (2024) results are more similar to ours. A possible reason is pre-enrichment from the nearby massive systems in the Justice League simulation as it simulates a LG-like environment. Another possibility is differences in the quenching time. The UFDs in Applebaum et al. (2021) appear to have more extended SFHs compared to ours (cf. Figure 11 in their article). Although mostly quenched by $z \sim 3$, there is a significant fraction of galaxies in their simulation with star formation lasting >1 Gyr. In contrast, our qDGs are mostly quenched completely before 500 Myr, with the exception of qDG2, which has a SFH extended to 1.5 Gyr. qDG2 has an average metallicity of [Fe/H] = –2.37, which is more consistent with observations. However, even the Applebaum et al. (2021) simulation still seems to quench the SF too rapidly compared to the UFD observations, in particular from Weisz et al. (2014).

4. Formation of Dark Matter Cores

Recent works have shown how stellar feedback, in particular from repeated supernova explosions, can transform the inner DM profiles of dwarf galaxies, thereby the central cusp is transformed into a core (e.g. Read & Gilmore 2005; Governato et al. 2010, 2012; Peñarrubia et al. 2012; Pontzen & Governato 2012; Madau et al. 2014; Oñorbe et al. 2015; Fitts et al. 2017; Mina et al. 2021). We expect the changes in the SFH and thus available feedback energy between the Superbubble run from Mina et al. (2021) and the RT run to alter the properties of the DM cores in the simulated dwarf galaxies. In Fig. 9, we show the DM density profiles of Bashful (top) and Doc (bottom) from our simulation. For comparison, the results of the Superbubble simulation from Mina et al. (2021) and a dark-matter only simulation are also plotted. It is clear that core formation still occurs in our simulation, but the core sizes are significantly smaller than in the Superbubble simulation. As in the Superbubble and Blastwave runs, the DM distribution is well described by a pseudo-isothermal density profile, defined as:

$$\rho_{\rm DM} = \frac{\rho_0}{1 + (r/r_{\rm c})^2}, \tag{3}$$

where ρ_0 is the central DM density and r_c is the core radius. The best-fitting pseudo-isothermal density profiles are also shown in Figure 9 (gray lines). At $z = 0$ the DM core sizes of Bashful and Doc are $r_c = 1.117 \pm 0.014$ kpc and 0.969 ± 0.014 kpc, respectively, which are about 3 (2) times smaller than those of the Superbubble runs for Bashful (Doc). In other words, the addition of radiative feedback decreases DM core sizes. The average central dark-matter densities within 150 pc, ρ_c(150 pc), for Bashful and Doc are 5.76×10^7M$_\odot$ kpc^{-3} and 4.69×10^7M$_\odot$ kpc^{-3}, respectively. This is in agreement with the data from Read et al. (2019), where the authors found that the central DM densities within 150 pc for local dwarf galaxies are below 10^8 M$_\odot$ kpc^{-3} if the galaxies have more extended star formation.

The reason for the reduced core sizes is likely due to the fact that Bashful and Doc have less bursty star formation in our

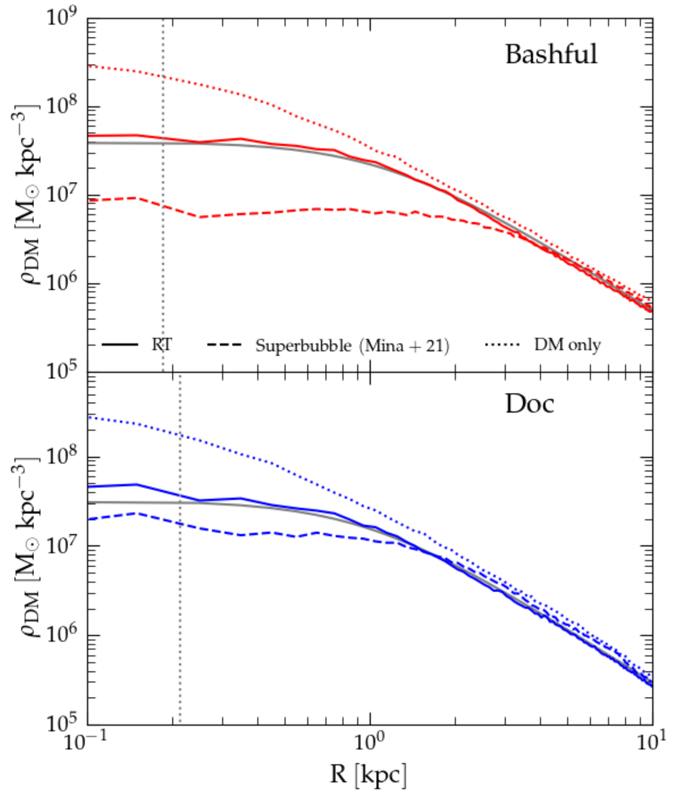

Fig. 9. Present-day DM density profile for the two most massive dwarf galaxies in the simulation, Bashful (top) and Doc (bottom). The solid lines represent the RT run, the dashed lines correspond to the Superbubble run (Mina et al. 2021), and the dotted line is the DM-only comparison run. The gray line shows the best-fitting pseudo-isothermal DM profile. The vertical dashed lines indicate the radii below which numerical convergence cannot be reached to two-body relaxation (Power et al. 2003).

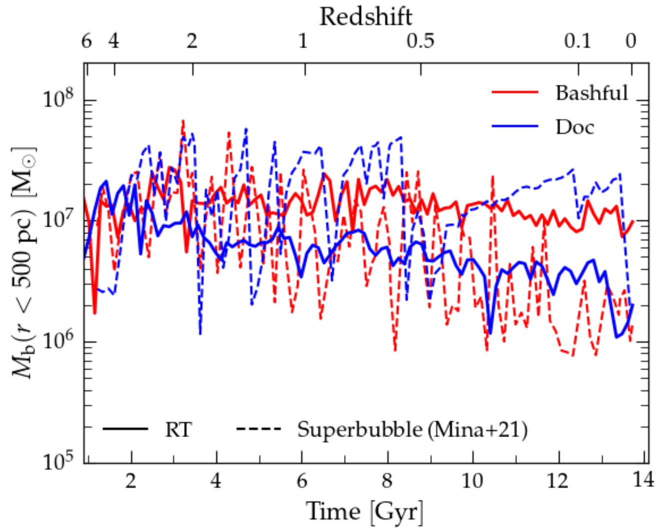

Fig. 10. Evolution of baryonic mass within the inner 500 pc of Bashful (red) and Doc (blue). Solid lines represent the RT run and dashed lines show the Superbubble run (Mina et al. 2021).

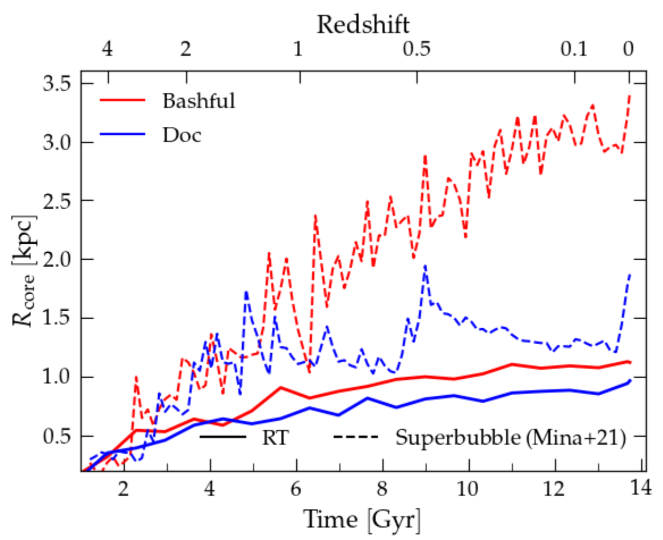

Fig. 11. Temporal evolution of the DM core radius for Bashful (red) and Doc (blue). Solid lines represent the RT run and dashed lines show the Superbubble run (Mina et al. 2021). The less bursty SFH and overall smaller stellar mass in the RT run results in significantly smaller DM cores.

simulation. As discussed in Section 3.4, a smoother SFR indicates that star formation is less clustered and the SN feedback is weaker. As a result, the fluctuations of central baryonic densities in our simulation are not as prominent as in previous SN-only runs. We illustrate this in Fig. 10, where we show the evolution of baryonic mass within the central 500 pc of Bashful and Doc for the RT and Superbubble runs. In the RT run, Bashful's central baryonic mass remains around 10^7 M$_\odot$ with variations of only about a factor of two. In contrast, Bashful in the Superbubble run show much larger fluctuations of its central mass, often exceeding an order of magnitude. A similar difference between the two runs is also seen in Doc. In the Superbubble simulation (as well as in the previous Blastwave simulation, not shown in Figure 10), the strong burst of SF nearly evacuates the gas in the central regions of these halos, followed by a quiescent phase during which the gas reservoir is replenished before the next SF episode repeats the cycle. Such cycles cause rapid and strong fluctuations of the central potential wells and eventually result in DM particles irreversibly moving to larger distances and thus form a core (Pontzen & Governato 2012). In the RT simulation these cycles still occur, but with smaller amplitudes, which leads to a smaller DM core. This is consistent with Azartash-Namin et al. (2024), where the authors compared a large number of dwarf halos within the Storm simulation and found clear positive correlation between the burstiness of SF and DM core slopes. Focusing back on Figure 10, it is interesting to note that unlike Bashful, Doc's central density in our simulation is on average lower than in the Superbubble simulation despite its SN feedback being weaker. This suggests radiative feedback may have played a role in preventing gas accretion and reaccretion after SN ejections, and this impact is more significant in lower-mass galaxies.

The milder baryonic mass fluctuations at the centre of the halo appear to correlate with the core size evolution, which is shown in Figure 11. Unlike the Superbubble run (dashed lines) and previous Blastwave runs (Figure 3 in Madau et al. 2014), the evolution of core sizes for both Bashful and Doc in our simulation is more monotonic: core formation starts at an early time, as in previous simulations, but there are no abrupt increases and decreases in core sizes within a short period of time. In previous SN-only simulations, a strong gas evacuation period is usually followed by a sudden increase in the size of the core, while rapid gas reaccretion causes the size of the core to decrease significantly due to adiabatic contraction, in which the DM halo compresses and becomes more cuspy when a large amount of baryonic matter is accreted at the centre (e.g. Sellwood & McGaugh 2005). With the amplitudes of both gas ejection and accretion reduced, our simulated galaxies have a smoother core size evolution. Nevertheless, in all simulations the dark-matter core is persistent and survives gas inflows from reaccreting previous outflows, and from merger events.

As in Mina et al. (2021), we estimate the minimum energy required for the cusp-core transformation and compare it to the total energy injected by Type II SNe ($\Delta E_{\rm SN}$). The minimum energy required for the cusp-core transformation can be estimated as $\Delta W/2 \equiv (W_{\rm core} - W_{\rm cusp})/2$ (Peñarrubia et al. 2012), where W is the gravitational binding energy of the DM halo, given by:

$$W = -4\pi G \int_0^{R_{\rm vir}} \rho_{\rm DM}\, M_{\rm enc}\, R\, {\rm d}R, \tag{4}$$

where G is the gravitational constant, $\rho_{\rm DM}$ is the DM density and $M_{\rm enc}$ is the total mass enclosed within radius R. Transformation from a cuspy to a cored DM profile is possible if $\Delta E_{\rm SN}$ is greater than $\Delta W/2$. At $z = 0$, ($\Delta E_{\rm SN}$, $\Delta W/2$) = (9.05×10^{56} erg, 5.04×10^{56} erg) for Bashful and (1.87×10^{56} erg, 9.09×10^{55} erg) for Doc. For both dwarfs, the available energy from SN explosions is still abundant, about twice that of the minimum energy needed for cusp-core transformation. The difference in DM mass between the hydrodynamic run and the DM-only run within the core radius, $\Delta M_{\rm DM} \equiv M_{\rm DM}^{cusp} - M_{\rm DM}^{core}$, is $1.41 \times 10^8 {\rm M}_\odot$ and $1.00 \times 10^8\, {\rm M}_\odot$ for Bashful and Doc, respectively. The ratio between $\Delta M_{\rm DM}$ and the stellar mass $M_\star$ roughly indicates how effective stellar feedback kinematically heats the DM. This "DM core removal efficiency" ($\Delta M_{\rm DM}/M_\star$), is 2.8 for Bashful and 9.9 for Doc. It seems that stellar feedback is more efficient to create cores in lower mass halos, until $M_\star$ become too small so that feedback is not sufficiently energetic (Peñarrubia et al. 2012; Read et al. 2019). However, our RT simulation appears to have a much smaller $\Delta M_{\rm DM}/M_\star$ compared to the SN-feedback only Superbubble run, which has $\Delta M_{\rm DM}/M_\star$ of 6.55 (19.39) for Bashful (Doc). Again, radiative feedback modulates the baryonic cycles and renders core formation less efficient.

The product of central DM halo density and the DM core radius, $\rho_0\, r_{\rm c}$, has been found to be remarkably constant over a wide range of galaxy types and a luminosity range of more than 14 magnitudes in the B band (e.g. Salucci 2019, and references therein). For example, Donato et al. (2009) found $\log(\rho_0 r_{\rm c}) = 2.15 \pm 0.2$ based on co-added rotation curves of spiral galaxies, mass modelling of individual (dwarf) galaxies, and galaxy-galaxy weak-lensing signals, with indications that the relation holds true for dSphs. Subsequent works found that the product $\rho_0\, r_{\rm c}$ of the Milky Way's dSphs is consistent with extrapolations from higher-mass systems (e.g. Salucci et al. 2012; Burkert 2015). In Figure 12, we compare $\rho_0\, r_{\rm c}$ of Bashful and Doc to the scaling relations from Burkert (2015) and Donato et al. (2009) and to disc dwarf galaxies from Karukes & Salucci (2017) and the dSph from Salucci et al. (2012). In addition, we compare results from Azartash-Namin et al. (2024) of the Storm Simulations. The higher central DM density and smaller core size of Bashful and Doc in the RT run make $\rho_0\, r_{\rm c}$ more consistent with the derived scaling relations of galaxies, while in both the Superbubble and Blastwave seven dwarf simulations this product is somewhat too low. However, there is considerable scatter

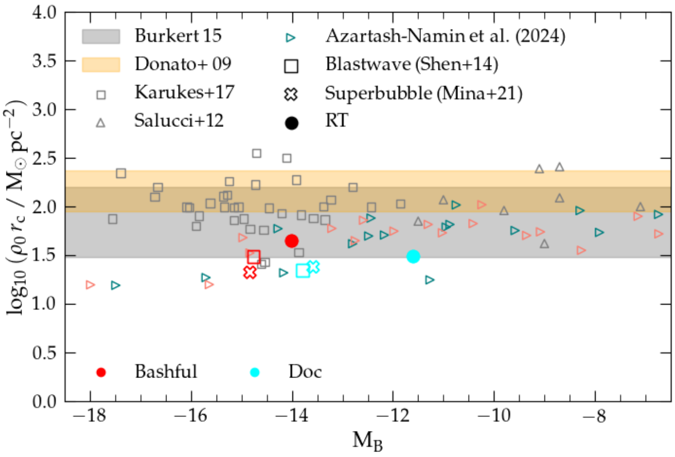

Fig. 12. Dark Matter core surface density ($\rho_0\, r_{\rm c}$) as a function of B-band magnitude of Bashful and Doc compared to disc dwarf galaxies (Karukes & Salucci 2017, gray squares), Milky Way dSphs (Salucci et al. 2012, gray triangles), the scaling relations from Donato et al. (2009, yellow shaded region), Burkert (2015, gray shaded region) and simulation data from Azartash-Namin et al. (2024) (teal and light red triangles for their blastwave and superbubble feedback simulations, respectively.

in the $\rho_0\, r_{\rm c}$-$M_{\rm B}$ relation in both observational data and simulations with a larger galaxy sample such as the Storm simulation, indicating other factors, such as environments and merger histories may play a role. Future RT simulations with a larger sample of dwarf galaxies in different environments are necessary to further understand the impact of radiative feedback on cusp-core transformation.

Our results are in agreement with many previous works in the literature, which demonstrated that impulsive baryonic outflows and inflows triggered by supernova feedback can dynamically heat DM and form DM cores in dwarf galaxies (e.g. Mashchenko et al. 2008; Governato et al. 2010, 2012; Oñorbe et al. 2015; Fitts et al. 2017). Adding radiative feedback in our simulation mainly reduces the strength of the baryonic cycle and thus decreases the DM core sizes. However, it is still under debate whether SN-feedback is sufficient for cusp-core transformation even for classical dwarfs. For example, no core formation was found in the APOSTLE simulations of the Local Group environment (Sawala et al. 2016) and the AURIGA simulations of MW-like halos (Bose et al. 2019), nor were DM cores found in isolated dwarf simulations from Revaz & Jablonka (2018) of halos up to virial mass of $\sim 10^{10}\, {\rm M}_\odot$. More recent work (Pandora Project) from Martin-Alvarez et al. (2023) simulated a $10^{10}\, {\rm M}_\odot$ halo with increasing complex physics, and concluded that SN feedback-only fails to form DM cores at $z \sim 3.5$, and radiative transfer and cosmic ray feedback contribute to the core formation, which is opposite to what we find here. Koudmani et al. (2025) investigate the impact of AGN feedback and cosmic rays on the cusp-core transformation in DGs, thereby, they find that AGN feedback promotes core formation directly by providing additional feedback energy and indirectly by suppressing early star formation. In their simulations cosmic rays suppress star formation and therefore indirectly reduces core formation, which is similar to the effect of radiation in our simulation.

In halos with $\Delta E_{\rm SN} > \Delta W/2$ such as Bashful and Doc, in principle, there is enough energy in SNe to "remove" the DM from the central region and lift it to a larger orbit

(Peñarrubia et al. 2012). However, in practice it is highly dependent on how much the SNe energy is coupled with the ISM, which regulates the episodic cycle of outflows and inflows, and the disturbance of the central gravitational potential well. Indeed, within the same framework of the seven dwarfs simulation with the same initial condition, same hydrodynamic and gravity solvers, and heating and cooling functions etc., variations of SN feedback model alone can alter the DM core size by 1–2 kpc. The superbubble model generates outflows with lower velocity and larger mass-loading factor than the previously adopted delayed cooling model (Keller et al. 2014), it creates larger fluctuations of the central mass density and thus larger DM cores. In general, although various subgrid SN feedback implementations can converge well and reproduce the global properties of galaxies, it has been shown that the outflow properties can look drastically different in idealised simulations (e.g. Smith et al. 2019) and cosmological comparison simulations such as AGORA (Strawn et al. 2024). Given the strong correlation between outflows and the core formation, it is not unexpected that DM core formation and core sizes vary significantly.

It is interesting to note that simulations with resolved Sedov–Taylor phase for SN feedback (Agertz et al. 2020; Gutcke et al. 2021; Deng et al. 2024) have also not reached consensus on cusp-core transformation. For the EDGE simulations, DM heating and flattening of the central profile are observed in the simulated halos, but the cusp-core transformation is not only caused by stellar feedback, but also by frequent minor mergers at later times, after the halos are quenched by reionisation at $z \sim 4$. However, late major mergers can regenerate the cusp (Orkney et al. 2021). Thus, the core formation depends on both SF activities and mass assembly histories. In contrast, LYRA simulations do not produce DM cores (Gutcke et al. 2022a). We note that these are simulations of UFDs with a halo mass $M_{\rm vir} \sim 10^9\,{\rm M}_\odot$ and a stellar mass typically less than 10^5–$10^6\,{\rm M}_\odot$, and SN-feedback may not provide sufficient energy to be solely responsible for cusp-core transformation. Moreover, as they are often quenched at a high redshift, the impact of assembly histories (major and minor mergers) can be significant, resulting in large scatter in DM core properties at $z = 0$. Nevertheless, it is a promising approach, and it would be interesting to also apply it to more massive dwarf galaxy simulations. Observations of inner DM content in this mass regime also have large uncertainties because many galaxies do not have HI gas or clean HI kinematics, and as such, it is difficult to measure the rotation curves.

For the fainter dwarf galaxies in our simulation, only Dopey, Grumpy, and qDG2 have marginally resolved DM cores ($r_{\rm c}$ = 0.290 kpc, 0.344 kpc and 0.490 kpc, respectively, after we apply the Power et al. (2003) criterion to estimate the radius within which the two-body relaxation time is shorter than the Hubble time. These three galaxies are among the most massive ones in the faint dwarf population and have stellar masses of several $10^5\,{\rm M}_\odot$, similar to the aforementioned work on UFD simulations. However, it is interesting that qDG3 does not have a resolved DM core, although it has a higher stellar mass than all the three galaxies that have cores. As qDG3 is quenched earlier ($z_{\rm SF,last}$ = 4.0, cf. Table 3), we speculate that even if a small core formed in this galaxy due to early SF activities, later merger events can transform it back to a cusp. This is in agreement with a recent study using the EDGE simulations by Muni et al. (2025), in which it was found that early SF quenching by reionisation is correlated with higher central DM density at $z = 0$. However, due to the limited resolution in our simulation, we do not perform further analysis of the faint dwarfs here and defer doing so to a future work.

5. The circumgalactic medium

The CGM contains crucial information on galaxy formation and baryonic cycles, and this is particularly important for the faintest dwarf galaxies with shallow gravitational potential wells. Although the less-bursty star formation rate (Section 3.4) and smaller DM cores (Section 4) indicate somewhat weaker galactic outflows driven by SNe in our simulation compared to previous simulations without RT, the extremely low stellar metallicities at $z = 0$ (Section 3.6) still suggest that our simulated galaxies lose most of the metals through outflows into the CGM and the IGM. Indeed, at $z = 0$, about 71.4% and 91.8% of total metals within $R_{\rm vir}$ for Bashful and Doc are outside the central discs, respectively. Mina et al. (2021) compared the properties of the CGM between the Blastwave simulation and the Superbubble run and found that the CGM is a sensitive probe for feedback models. In this section, we investigate the impact of radiative transfer in our simulation on the CGM gas and metal distributions.

Figure 13 shows the total metal column density ($N_{\rm z}$) at redshift z = 6, 3, 1 and 0 in our simulation (first row), as well as the Superbubble and Blastwave simulations (second and third row, respectively). It is clear that galactic outflows eject a substantial amount of metals into the CGM. At $z = 0$, the total metal column density in the central region in our simulation appears to be smaller than that of the Superbubble run. However, the extent of the metal “bubble”, defined as the impact parameter (i.e. projected distance in 2D) where the covering fraction of $N_{\rm z} > 10^{12}\,{\rm cm}^{-2}$ decreases below 50%, is 334 kpc, approximately four times the virial radius of Bashful. This is slightly smaller, but comparable to the metal extent in the simulation with superbubble feedback (4.7 $R_{\rm vir}$) but much smaller than the metal extent produced in the blastwave simulation (16 $R_{\rm vir}$). As discussed in detail in Mina et al. (2021), and also in Keller et al. (2014), the superbubble feedback model typically generates relatively slower winds but with a higher mass-loading factor compared to the delayed cooling blastwave approach, resulting in a less extended metal distribution.

The fact that our RT simulation has a comparable CGM metal extent to the superbubble simulation may seem contradictory to our previous results, namely radiative feedback results in less powerful galactic outflows and the galaxies have smaller stellar masses. One may expect the CGM metals to be less spread out. However, the build-up of the metals in the CGM throughout cosmic history varies significantly between simulations. At high redshift, our RT simulation has a more extended metal distribution around each individual subhalo than the Superbubble simulation, and the difference is more obvious towards earlier times (see e.g. the first column of Figure 13). This is likely due to the fact that the RT simulation has predominantly early star formation, especially for the faint galaxies with $M_{\rm h} < 10^{10}\,{\rm M}_\odot$. These tiny halos have very shallow gravitational potential wells, where the galactic wind can easily pollute the surrounding CGM. It is worth noting that, by $z = 3$, the CGM metal density appears to be peaked at the centres of the two main halos (the progenitors of Bashful and Doc) and monotonically decreasing outwards, but it is clear from the evolution that the contributions from the satellites are non-negligible, if not dominant, at larger distances ($\gtrsim R_{\rm vir}$) from the galaxy centres. This is typical for high redshift systems (e.g. Shen et al. 2012), which makes it difficult to interpret CGM observations because usually only the central, more massive galaxies are observed.

In Figure 14, we compare the column densities of commonly observed ionisation species H I, C IV, O VI and Si II between the RT simulation and the Superbubble simulation. In Figure 15,

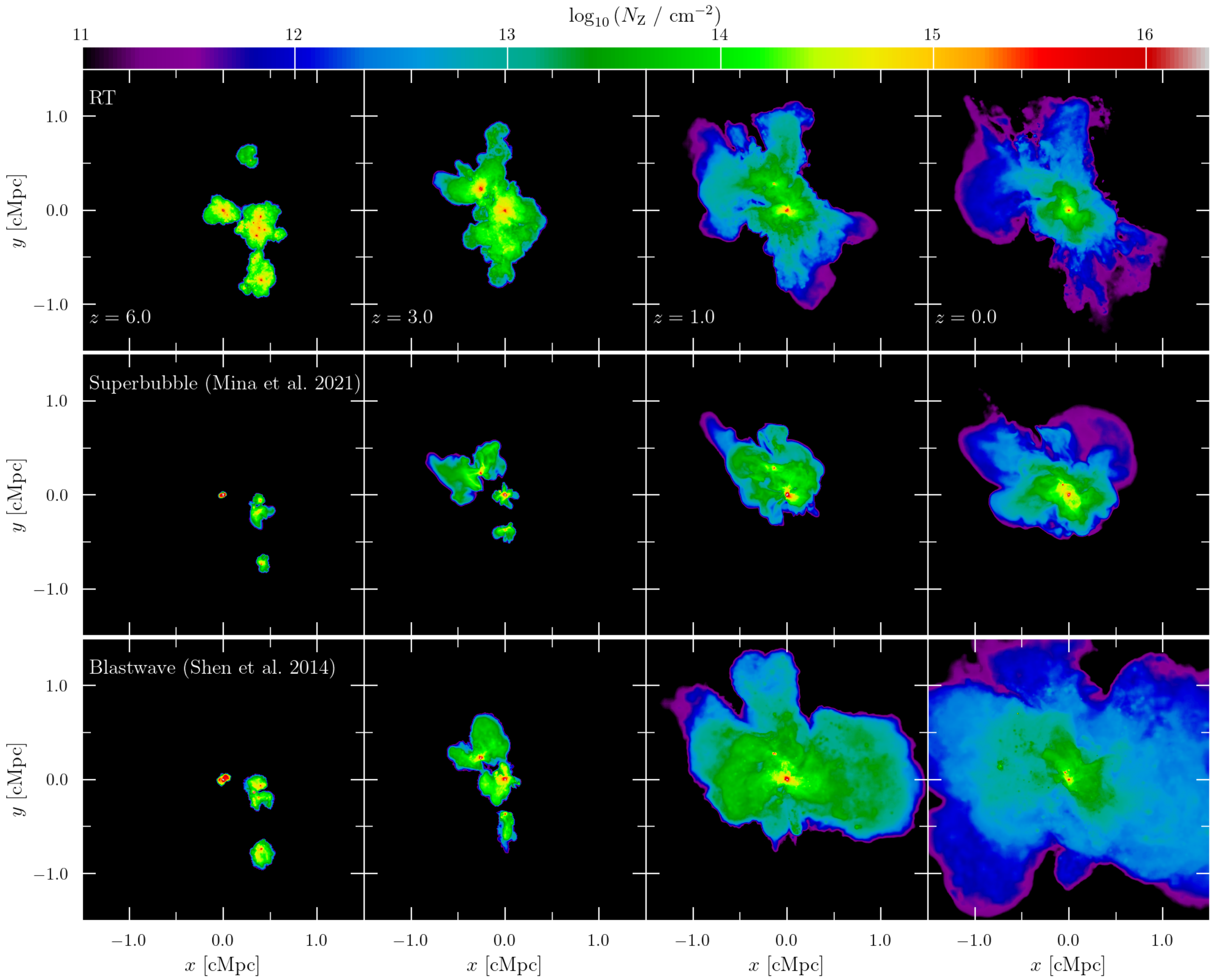

Fig. 13. Metal distribution through cosmic time from z = 6 to z = 0 for the RT (top), Superbubble (middle), and Blastwave (bottom) runs. Metals in the RT run are distributed over a greater area ,as stars are formed in a greater number of small progenitor halos.

we show the 1D column densities of these ions as a function of the impact parameter normalised by the virial radius ($b/R_{\rm vir}$) of Bashful, together with recent observations of local dwarf galaxies. The H I abundance is directly computed from the non-equilibrium chemistry solver coupled with radiative transfer (cf. Section 2). The abundances of metal ions are calculated particle by particle using the photonionisation code CLOUDY (Ferland et al. 2017), with the incident radiation spectrum from the RT simulation itself[2]. To investigate the impact of the incident radiation on ion abundances, we also calculate the abundances assuming a uniform z = 0 UV background from Haardt & Madau (2012), which is commonly used when post-processing simulations (including the Blastwave and Superbubble simulations) for comparison with CGM observations. The column density along each line of sight (LOS) is calculated using the analysis tool from Shen et al. (2013), by adding the contributions of particles weighted by a 2D projection of the SPH smoothing kernel.

[2] We extended the spectrum with three additional power-law segments between 0.5–1 keV, 1–5 keV and 5–10 keV following the Haardt & Madau (2012) UVB spectrum.

5.1. HI distribution

For the 1D H I distribution at z = 0, on the CGM scale ($b/R_{\rm vir} \gtrsim 0.25$), there is no significant difference between the RT (red curves in Figure 15) and the Superbubble run (blue curves). Neutral hydrogen is ubiquitous in all simulated galaxies, and rather insensitive to RT or feedback models. The similarities at larger distances can be explained by the fact that both simulations use the same Haardt & Madau (2012) UVB model, which dominates the radiation field at distances beyond ≈25 kpc or $b/R_{\rm vir} \gtrsim 0.30$ at z = 0. The median N(H I) at $b = R_{\rm vir}$ is about 10^{14} cm^{-2}, and the covering fraction ($C_{\rm f}$) of N(H I) > $10^{13.5}$ cm^{-2} (a common detection threshold, corresponding to an equivalent width EW ≳100 mÅ) is almost 100% within the virial radius, which is in good agreement with observations of isolated dwarf galaxies (Prochaska et al. 2011; Liang & Chen 2014; Bordoloi et al. 2014; Burchett et al. 2016; Johnson et al. 2017; Zheng et al. 2020, 2024; Mishra et al. 2024). For example, Zheng et al. (2024) compiled a sample of 45 isolated dwarf galaxies with the HST/COS data, and found that the H I detection rate within R_{200} is about 89% in the CGM. Liang & Chen (2014) investigated 195 galaxy-QSO

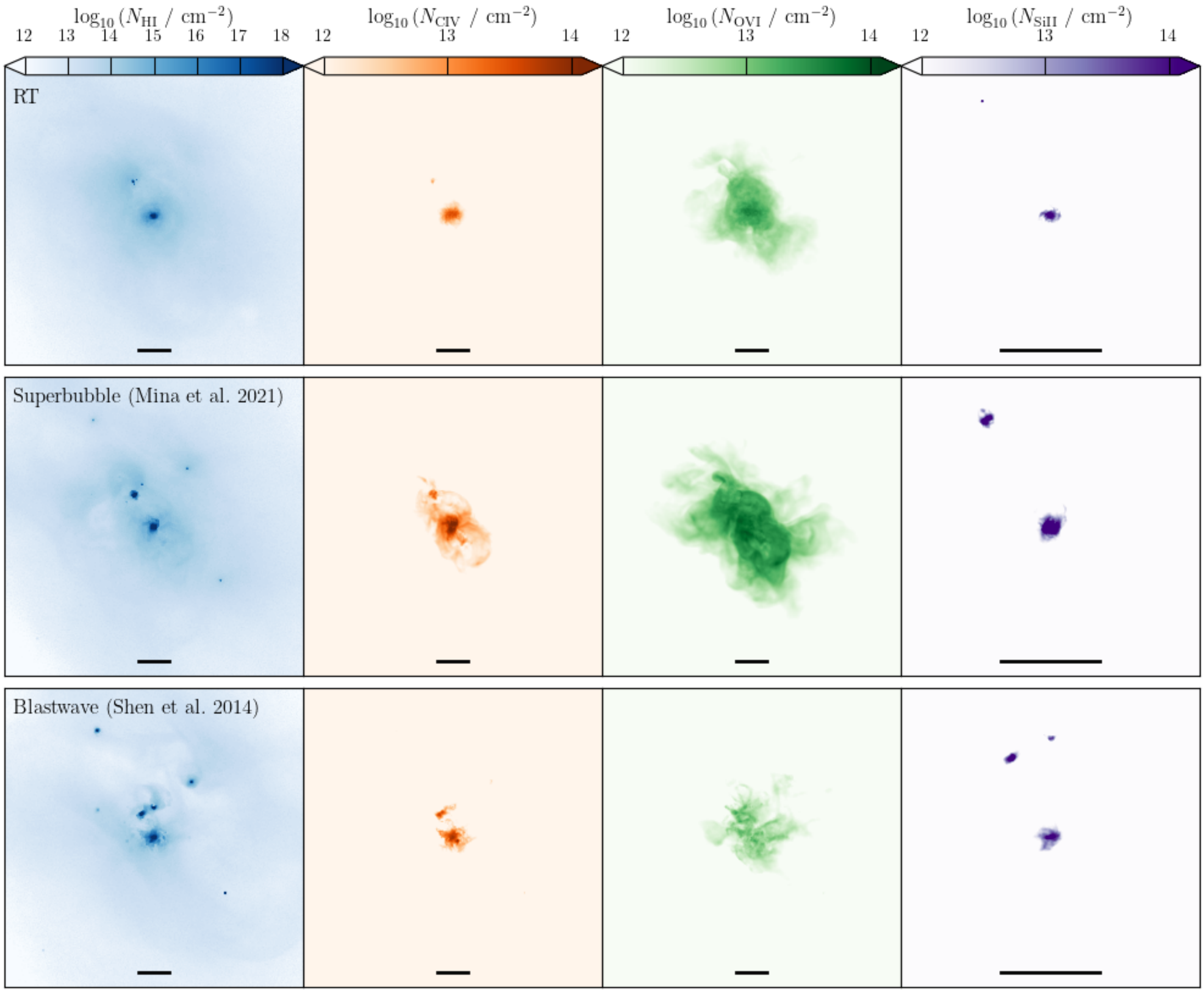

Fig. 14. Column density of H I, C IV, O VI, and Si II (from left to right) in a cube with a side length of 1 Mpc (300 kpc for SiII) at $z = 0$ for the RT , Superbubble , and Blastwave runs (top to bottom) of the group of DGs centred on Bashful. The black line in each panel indicates a length of 100 kpc.

pairs and found H I detection rate of 100%. Unlike more massive galaxies, where the neutral hydrogen in the CGM exists in a clumpy structure (e.g. Nelson et al. 2020; Decataldo et al. 2024), the H I around dwarf galaxies has a rather smooth distribution. The CGM is generally highly ionised, with a H I fraction ($f_{\rm HI}$) of about 10^{-2} at 0.1 $R_{\rm vir}$), which decreases to 3×10^{-5} at the virial radius. To interpret the observational data, the authors in Zheng et al. (2024) explored two empirical models for the CGM gas around a galaxy with $M_\star = 10^{8.3}\,{\rm M}_\odot$, both of which reproduce the observed N(H I) distribution. Model A with lower gas density ($n_{\rm H}(r)$) and a steeper profile, but higher volume filling fraction ($f_{\rm V} \equiv V_{\rm cool}/V_{\rm total}$) of cool (T < 10^4 K) gas, and Model B with higher gas density and a shallower profile, but with lower volume filling fraction. The former predicts lower C II (and other "low ions") column densities and higher C IV columns, and the latter is the opposite. In our simulation, the volume filling fraction of the cool gas is generally not very high, ranging from 0.033 at 0.1 $R_{\rm vir}$ to 3.4×10^{-5} at $R_{\rm vir}$, but the CGM has relatively high density $n_{\rm H}$ ranging from $7 \times 10^{-4}\,{\rm cm}^{-3}$ at 0.1 $R_{\rm vir}$ to about $10^{-5}\,{\rm cm}^{-3}$ at $R_{\rm vir}$. Therefore, our simulated galaxy has general CGM properties similar to Model B, although with somewhat steeper profiles for $n_{\rm H}$ and $f_{\rm V}$.

Although the CGM H I distribution is similar in all runs, at a smaller impact parameter ($b/R_{\rm vir} \lesssim 0.25\,R_{\rm vir}$, i.e. the ISM and the CGM close to the disc) the RT run has smaller H I column densities. This is the case for Bashful, but particularly obvious for Doc (see Figure 14), where the H I in the ISM appears to be "cleared out". In fact, the total mass of H I within Doc's virial radius started to decrease steadily below $z \sim 0.3$, and at $z = 0$ it has dropped by an order of magnitude, with $M_{\rm HI} = 6.7 \times 10^5\,{\rm M}_\odot$ (cf. Table 2). Since Doc is merging into Bashful towards the end of the simulation, one may expect that ram-pressure stripping plays a role (Putman et al. 2021). However, the total gas mass in Doc does not have a substantial decrease towards $z = 0$, indicating that the gas is mostly photoionised by internal and external radiation.

We emphasise that the weak dependence of CGM H I distribution on supernova and radiative feedback *only applies to low redshift ($z \lesssim 1$).* The H I distribution is drastically different between the RT run and the Superbubble run at high redshift. This has been illustrated in Figure 3, and we show the 1D N(H I) versus $b/R_{\rm vir}$ at various redshifts in Figure 16. Due to the fact that reionisation completes much later in the RT simulation than in the Superbubble run (cf. Section 3), gas remains largely neutral

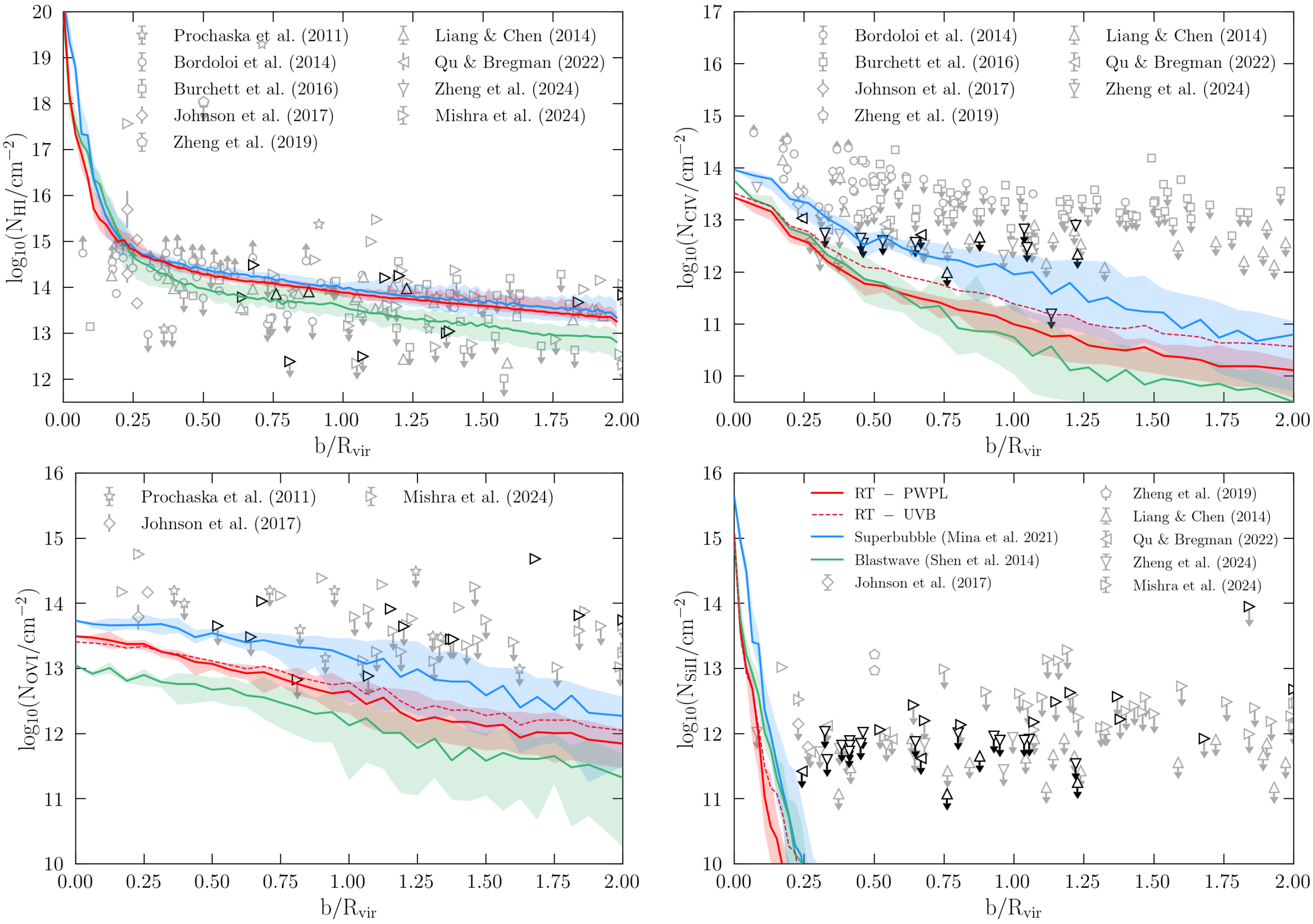

Fig. 15. Present-day column density as a function of impact parameter scaled with the virial radius of Bashful ($b/R_{\rm vir}$) of H I, C IV, O VI, and Si II (top left to bottom right) for the RT (red), the Superbubble Mina et al. (2021) (blue), and the Blastwave Shen et al. (2014) (green) simulation. The solid line indicates the median, and the shaded region corresponds to 1σ scatter. For metal ions, the red lines indicate results where the ionisation states are calculated particle by particle using the PWPL reconstructed spectrum (from the simulation) with an extension from 500 eV to 10 keV in the CLOUDY (Ferland et al. 2017) calculation. The red dashed line (RT-UVB) shows results where the ionisation states are computed assuming photoionisation equilibrium with the uniform UVB from Haardt & Madau (2012) (although the element abundances, density, temperature positions etc. are from the RT simulation), similar to what has been done with the Superbubble and Blastwave simulations. H I data are extracted directly from the simulation from the non-equilibrium chemical network. The observational data points from various CGM surveys are indicated with different legends. Darker symbols indicate the lowest mass halos with $M_{200} \leq 10^{10.5}$ $M_\odot$.

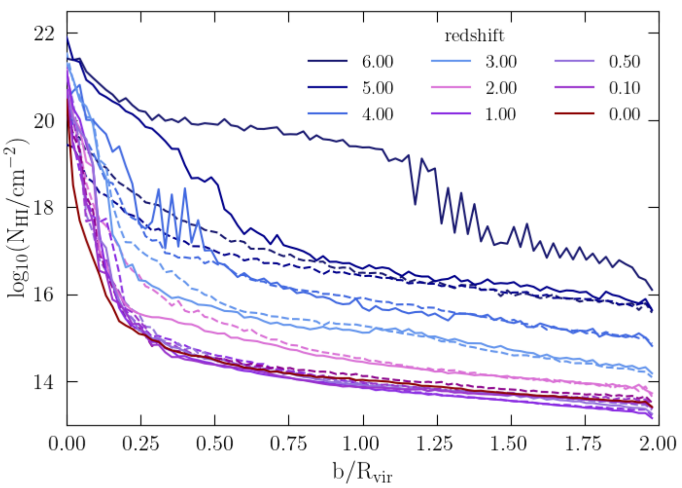

Fig. 16. One-dimensional H I column density distributions at different redshift ($z = 6, 5, 4, 3, 2, 1, 0.5, 0.1, 0$) as a function of impact parameter scaled with the virial radius of Bashful ($b/R_{\rm vir}$). Solid and dashed lines correspond to the RT and Superbubble run, respectively.

around the progenitor of Bashful in the RT simulation, leading to a much higher H I column of $\gtrsim 10^{20}$ cm^{-2} within 1 $R_{\rm vir}$ at $z = 6$, similar to the damped Lyα systems (DLAs) (Wolfe et al. 2005). With the completion of reionisation, the two runs start to converge at large distances, but the difference takes an opposite trend close to the galaxy at intermediate redshift ($z \sim 2$–3): the RT run has a lower N(H I) than the Superbubble run, likely because of the radiative feedback from Bashful. The difference is largest at the inner CGM, around 0.25 $R_{\rm vir}$, indicating a non-negligible escape fraction of ionising radiation.

5.2. Metal ion distributions

The distribution of moderately ionised C IV is also extended but is generally below the detection limit. Observationally, non-detection is often associated with lower-mass dwarf galaxies. For example, Burchett et al. (2016) found that C IV detection is more associated with galaxies with $M_\star > 10^{9.5}$ $M_\odot$ but rarely with smaller systems. Zheng et al. (2024) divided their sample of dwarf galaxies into different mass bins, and found most non-detection of C IV for $M_{200} = 10^{10} - 10^{10.5}$ $M_\odot$. Since Bashful has a virial mass $M_{\rm vir} = 3.5 \times 10^{10}$ $M_\odot$ and stellar mass only

$M_\star = 4.5 \times 10^7\ M_\odot$, it is not unexpected that our predictions are below the detection limit. More quantitatively, the covering fraction of N(C IV) > $10^{13.5}$cm^{-2} is only 2% within $R_{\rm vir}$, much below the observational findings of 22% from Zheng et al. (2024) and 23% from Johnson et al. (2017). This may again be due to the simulated galaxy being a smaller system compared to the average stellar mass in observed galaxies. The trend of decreasing C IV column density in the CGM of smaller galaxies is also seen in simulations. For example, Zheng et al. (2024) used the EAGLE simulation (Schaye et al. 2015) and went through the same analysis as the observational data and showed smaller H I, C IV, and C II column densities in lower-mass galaxies. A similar trend is also found in Piacitelli et al. (2025) with the Marvelous Dwarf and Marvelous Massive Dwarf simulations. It is clear that more statistics are needed in both observations and simulations for the CGM of the faintest dwarf galaxies $M_\star < 10^8\ M_\odot$ to make more direct comparisons.

The distribution of highly ionised O VI in our simulation is more extended than C IV, although it is also mostly below the detection limit for $b/R_{\rm vir} \gtrsim 0.25$, and this is also seen in Piacitelli et al. (2025) and in the FIRE-2 simulation (Li et al. 2021). Observationally, the highly ionised O VI is more commonly detected compared to other metal ions, and the detected O VI column densities are generally higher than those in our simulation (Prochaska et al. 2011; Johnson et al. 2017; Mishra et al. 2024) even for galaxies with similar masses. Thus, our simulation underpredicts O VI. As suggested in Piacitelli et al. (2025), this can be due to not enough metals being ejected into the outer CGM or the O VI-bearing phase being underpredicted in the simulation, or both. While there is still the possibility the former occurs, the stellar metallicities provide constraints on how much metals can be ejected. Moreover, the observed kinematics of O VI absorbers show that the gas is largely bound (Mishra et al. 2024) (at least for low redshift samples), indicating that it cannot travel to large distances. Therefore, it is more likely the oxygen is in a different ionisation state. In fact, in our simulation the CGM oxygen budget is dominated by O V and O VII, rather than O VI. The ionisation fraction of O VI increases with distance but reaches a plateau of ~0.2 at $r > 0.6\ R_{\rm vir}$. This is much smaller than that of O VII, which is ~0.5–0.6 at 1 $R_{\rm vir}$. Moreover, the gas ionisation states depend on not only gas density and temperature, but also the radiation field. We discuss the impact of RT on CGM metal ions in Section 5.3.

Unlike the H I and the "high ions", the distribution of Si II is very compact. The median N(Si II) drops below $10^{13.5}$ cm^{-2} only at 0.1 $R_{\rm vir}$, indicating that Si II is mainly within the ISM rather than the CGM (cf. Figure 14). This is generally in good agreement with observations, which rarely detect "low ions" such as Si II, Si III and C II in the CGM of dwarf galaxies, and this is especially true for lower mass dwarfs (Johnson et al. 2017; Zheng et al. 2024). As we discussed in Section 5.1, the CGM in our simulation is highly ionised. The gas is generally smooth and lacks the clumpy cold clouds that are often seen in the CGM of more massive galaxies (Decataldo et al. 2024) or in high redshift systems (e.g. Shen et al. 2013), which give rise to low ion metal absorbers (e.g. Werk et al. 2013; Prochaska et al. 2017).

5.3. Impact of RT on CGM metal distributions

Compared to the Superbubble simulation from Mina et al. (2021), our RT simulation shows smaller column densities of C IV, O VI, and Si II. Several factors may have contributed to this. Firstly, there are fewer metals in general that are ejected into the CGM of Bashful and Doc, mainly because the galaxies

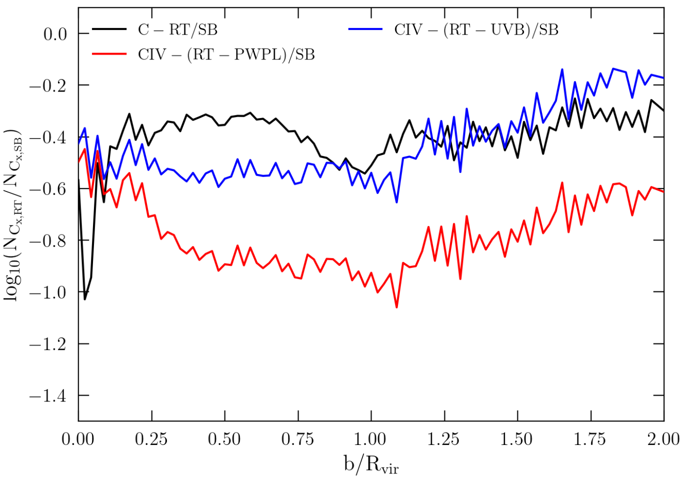

Fig. 17. Column density ratios of carbon ion species between the RT run and the Superbubble simulation without RT. The black line indicates the total carbon ratio. The blue line shows the ratio of C IV calculated with CLOUDY, assuming a uniform extragalactic UVB. The red line indicates the C IV ratio of the two runs; in the RT run, the abundance is computed using the radiation field from the simulation.

have a smaller stellar mass with radiative feedback. In particular, Bashful's stellar mass in our simulation is only about one-third of that in the Superbubble simulation. This effect can be seen in Figure 13 ($z = 0$ panels), where the total metal column $N_{\rm Z}$ in the CGM near the galaxy is smaller in the RT run than in the Superbubble run. More quantitatively, Figure 17 shows that the total carbon column density (black line) in the RT run is about 0.3–0.5 dex below the Superbubble run, which corresponds to a 50% to 70% reduction in total carbon. This is consistent with the stellar mass differences in the two runs.

In addition to suppressing star formation and consequently reducing total metal production, stellar radiation can directly affect the ionisation states of the gas and abundances of metal species. It is interesting that, if we use the radiation spectra from the radiative transfer calculation, the abundance of C IV is further reduced (red line) by approximately 0.5 dex compared to the results obtained from CLOUDY calculation assuming the usual $z = 0$ UVB (blue line). After investigating other species of carbon ions, we find that the most abundant ions are C V and C VI. The ionisation energy of C IV is about 64.5 eV, which is not subject to strong absorptions from the most abundant H I in the ISM (e.g. Baumschlager et al. 2024). Thus, it appears that the hard photons that leak from the galaxy ionise C IV to higher ionisation states and cause significant reduction in C IV abundances, even though the star formation rate in Bashful at $z = 0$ is not very high (~$2 \times 10^{-3}\ M_\odot\ {\rm yr}^{-1}$). Similarly to C IV, the abundances of low ion Si II and high ion O VI are impacted by the same effect of being ionised to higher states. For Si II, the column density decreases rapidly towards a larger impact parameter, but the effect can still be seen at $b/R_{\rm vir} \gtrsim 0.1$. The suppression of O VI column density due to local radiation is generally not as prominent as for C IV, most likely because the flux of X-ray photons capable of ionising O VI (138 eV) is low in stellar spectra.

Our results show that it is important to model the ionising radiation spectrum accurately when creating synthetic observations for the CGM. In particular, photons with energy much higher than 13.6 eV can escape the ISM relatively easily and impact CGM ionisation states. The impact of local radiation on CGM observables is investigated in several recent studies, but is mostly focused on more massive galaxies. For instance, Oppenheimer et al. (2018) performed zoom-in simulations from the EAGLE volume with non-equilibrium chemical network (Richings et al. 2014), and found that hard radiation from flickering AGN can boost O VI column densities around $L_\star$ halos due to the long recombination timescale. More recently, Zhu & Springel (2024) simulated five Milky Way-like systems from the Auriga project with radiative feedback, and found that local stellar radiation dominates the radiation field within the virial radius at all redshift, and can suppress H I and Mg II column densities in the inner halo. The O VI column density is not significantly affected by radiation due to the lack of hard photons, which is similar to what we find. However, Holguin et al. (2024) performed Monte-Carlo RT on 12 FIRE simulations and concluded that at low redshift, local stellar radiation is subdominant beyond 0.2 $R_{\rm vir}$ around MW-like halos, although it can be important at cosmic noon. As faint dwarf systems differ significantly from MW-like systems in terms of environment, assembly history, SFH, escape fraction, and CGM properties such as density, temperature, and substructures, we cannot directly compare our results with the simulations of more massive galaxies, but we note that local radiation can potentially have stronger impact on the CGM of dwarf galaxies than to more massive systems, because the ISM of dwarf galaxies is more prone to mechanical feedback events, leading to higher escape fractions (e.g. Kimm & Cen 2014).

Of course, the impact of radiation on the CGM is not only on the observables; the changing of the ionisation states of metal ions would fundamentally alter the metal cooling rate, and consequently the dynamics of gas accretion and galaxy evolution (e.g. Obreja et al. 2024). Ideally, simulations should incorporate on-the-fly RT coupled with non-equilibrium chemical solvers for metal ions in addition to the primordial species (e.g. Katz 2022), but this approach can be computationally prohibitive for cosmological simulations that evolve to $z = 0$. Alternatively, one can assume ionisation equilibrium, and use pre-tabulated tables with varying radiation field parameters (Gnedin & Hollon 2012). We defer a more detailed study on the impact of local radiation field on metal cooling and gas dynamics in a future work.

6. Conclusions

We have presented the results from a cosmological zoom-in simulation of a small group of field dwarf galaxies. The simulation was performed with the GASOLINE2 code coupled with the on-the-fly radiative transfer algorithm TREVR2 (Wadsley et al. 2024) and evolved to $z = 0$. Stellar radiation was included according to an age-dependent spectral energy distribution calculated from STARBURST99 (Leitherer et al. 2014), and a redshift-dependent UV background radiation (Haardt & Madau 2012) was modelled with background particles. The UV background was turned on at $z = 15.1$ and propagated towards the simulation volume. The ionisation, heating, and cooling of primordial gas were computed with a non-equilibrium chemical network and coupled with RT, but radiative cooling from metal lines were calculated with the CLOUDY table while assuming photoionisation equilibrium with the uniform UVB. The initial condition, resolution, and other galaxy formation physics, such as star formation, metal enrichment, and supernova feedback were identical to the seven dwarfs simulation by Mina et al. (2021), which we call the Superbubble run in comparison. We also compared our simulation with the first version of the seven dwarfs simulation from Shen et al. (2014), which uses a delayed cooling model for SN feedback, and we refer to it as the Blastwave run. The main focus of this work was to investigate the impact of radiation in dwarf galaxy formation and the interplay between radiative feedback, star formation, and supernova feedback in shaping galaxy properties and the surrounding CGM.

In total, 12 galaxies formed within our simulation volume. Among them are two luminous dwarf galaxies, Bashful and Doc, which reside in halos with $M_{\rm vir} > 10^{10}\,{\rm M}_\odot$. These galaxies are gas-rich and star-forming towards $z = 0$, although Doc's ISM is largely photoionised by internal and external radiation towards low redshift. Two faint dwarf galaxies, Dopey and Grumpy, formed within halos of mass $10^9\,{\rm M}_\odot < {\rm M}_{\rm vir} < 10^{10}\,{\rm M}_\odot$. They have stellar masses of several $10^5\,{\rm M}_\odot$ and completed star formation by $z = 3.2$ and thus have only old stellar populations. These four galaxies also formed in the original Blastwave simulation. There is an additional population of eight quenched galaxies that have all accreted into Bashful's halo by $z = 0$, which we label as qDG1-8. These galaxies reside in halos with masses varying from $10^6\,{\rm M}_\odot$ to several $10^8\,{\rm M}_\odot$ and have typical stellar masses from $10^4\,{\rm M}_\odot$ to a few times $10^5\,{\rm M}_\odot$. Their DM halos are strongly stripped during the accretion to Bashful. Most of the star formation occurred at $z \sim 4$. These qDGs, together with Dopey and Grumpy, have luminosities and SFHs similar to the observed UFDs in the Local Group.

We summarise the main findings of this work as follows:

– The formation of Dopey, Grumpy, and qDGs is strongly influenced by cosmic reionisation. The main reason these galaxies have early star formation is that the ionising background radiation requires a finite timescale to propagate into the simulation volume. Although UVB is "turned on" at $z = 15.1$, the IGM in the simulated volume is not fully ionised before $z \sim 4$, leaving enough time for gas within the smallest halos to remain cold, condense, and form stars. This propagation time delay is captured in our RT run, but not in the previous Superbubble and Blastwave simulations, where the uniform UVB is turned on instantaneously within the whole simulation region;
– Radiative feedback decreases the total stellar mass of the two most massive galaxies, Bashful and Doc, by a factor of two to three. It also results in less bursty star formation rates (SFR) than in the Superbubble simulation. Similar to other studies with RT, photoionisation heating preconditions the ISM such that star formation is less clustered, which in turn results in weaker collective SN feedback and outflows. The SFH of both classic and UFDs are consistent with observations;
– The simulated galaxies have many properties that are generally consistent with observed scaling relations, including the SMHM ($M_\star - M_{\rm h}$) relation, mass-size ($M_\star - r_{1/2}$) relation, and luminosity-velocity dispersion ($M_{\rm V} - \sigma_{\rm los}$) relation. Compared to the Superbubble simulation, for Bashful and Doc, radiative feedback reduces the stellar disc sizes, possibly because of the earlier SFHs and reduced galactic outflows. The velocity dispersion is not strongly impacted by RT, but dynamic interactions and tidal stripping significantly reduce the stellar velocity dispersion of qDGs;
– The simulated dwarf galaxies are extremely metal poor, with the average [Fe/H] ranging from –3.3 to –1.5. Although the stellar metallicity (indicated by [Fe/H]) of Bashful and Doc are in good agreement with the observed LZR, the stellar metallicity of the faint dwarf galaxies (Dopey, Grumpy and the qDGs) with V-band luminosity $L_{\rm V} < 10^6\,{\rm L}_\odot$ is systematically lower than the observations of UFDs. The MDF of

these galaxies peaks at [Fe/H] ~ -3.5, which is about an order of magnitude lower than observations from Fu et al. (2023). This may indicate that our SN feedback ejects too much metals but can also be due to the uncertainties in iron yields from both Type Ia and Type II supernova at high redshift. The actual average metallicity ($Z/Z_\odot$) of the faint dwarf galaxies are more consistent with the MZR;

– At $z = 0$, the DM cores of Bashful and Doc are respectively about 1.12 kpc and 0.96 kpc in size, which is about three(two) times smaller than those in the Superbubble run for Bashful (Doc). The average central DM densities within 150 pc are $5.8 \times 10^7\,M_\odot kpc^{-3}$ and $4.7 \times 10^7\,M_\odot kpc^{-3}$, respectively, which are in agreement with data from Read et al. (2019). Compared to the Superbubble simulation, the baryonic mass fluctuation at the galaxy centres (<500 pc) are milder due to less impulsive galactic winds and preventive feedback from local stellar radiation. This leads to less fluctuation in the central gravitational potential well and consequently less DM heating, and smaller cores. The DM core formation starts early, but unlike previous simulations, the core size growth is rather smooth and without abrupt changes that are associated with rapid outflows and inflows;

– Among the fainter dwarf galaxies, only Dopey, Grumpy, and qDG2 have marginally resolved DM cores, with r_c = 0.29 kpc, 0.34 kpc, and 0.49 kpc, respectively. These three galaxies have stellar masses of several $10^5\,M_\odot$ and are therefore among the most massive in the faint galaxy sample. Our results are in agreement with only some higher resolution UFD simulation where SN feedback is resolved (e.g. Agertz et al. 2020). Moreover, it is interesting that qDG3 does not have a resolved DM core, despite it being more massive than the three galaxies that formed cores. Since this galaxy is quenched early, it suggests that dynamic interactions such as mergers can have non-negligible impact on DM cusp-core transformation;

– The extent of the metal-enriched volume in the CGM in our RT simulation is comparable to that in the Superbubble simulation at $z = 0$, about four times that of the virial radius of Bashful. This confirms previous findings that dwarf galaxies are very efficient CGM polluters. However, due to the early SFH in our simulation (before reionisation is completed), at high redshift ($z \gtrsim 3$) the CGM metal extent is much larger than the ones in previous seven dwarfs simulations. Even at $z = 0$, the contribution from satellite progenitors to the CGM metals at large distances is non-negligible;

– The H I distribution on the CGM scale (with impact parameter $b \gtrsim 0.25\,R_{\rm vir}$) is ubiquitous and rather insensitive to RT or feedback models. At $R_{\rm vir}$, the median column density N(H I) is about $10^{14}\,{\rm cm}^{-2}$ with a unity covering fraction, which is in good agreement with observations. The CGM is highly ionised, with a relatively low volume filling fraction of cold neutral gas. At the inner halo or ISM scale, however, local stellar radiation decreases H I column densities. In particular, the impact of photoionsation heating combined with ram-pressure stripping causes Doc to lose a majority of its ISM close to $z = 0$;

– The distributions of high ions such as C IV and O VI are extended, whereas low ions such as Si II are very compact, which declines sharply beyond the ISM scale (>0.1 $R_{\rm vir}$). Nevertheless, the metal column densities are generally below the observational detection limit, especially at larger distances. The covering fractions within the virial radius are also smaller compared to observations. However, it is unclear whether there is a true discrepancy or it is due to the fact that the observation data are for more massive dwarf galaxies, with the median stellar mass an order of magnitude larger than Bashful;

– Compared to the Superbubble simulation, our simulation resulted in smaller column densities of C IV, O VI and Si II. The main reasons are 1) the total metal production is reduced because radiative feedback suppresses star formation in Bashful and Doc, 2) Photons with energies higher than hydrogen ionisation can escape the ISM and further ionise metal ions in the CGM, particularly the moderately ionised C IV, which is reduced by approximately 0.5 dex compared to the results obtained from CLOUDY calculations assuming a uniform UVB. Thus, it is important to model the ionising radiation spectrum accurately when creating synthetic CGM observations.

These findings demonstrate that radiative transfer significantly influences dwarf galaxy formation, regulating star formation, feedback processes, and the emergence of observable properties. Our results highlight the need for future simulations to incorporate full radiative feedback to accurately model the formation of faint galaxies in the early Universe.

Acknowledgements. We thank the anonymous referee for detailed comments that help to improve the manuscript. B.B. and S.S. acknowledge the support of the Research Council of Norway through the NFR Young Research Talents Grant 276043. S.S. and R.W. acknowledge support from the European High Performance Computing Joint Undertaking (EuroHPC JU) and the Research Council of Norway through the funding of the SPACE Center of Excellence (grant agreement No. 101093441). Parts of the computations were performed on resources provided by Sigma2 – the National Infrastructure for High-Performance Computing and Data Storage in Norway. BWK acknowledges support from the Space Telescope Science Institute, which is operated by the Association of Universities for Research in Astronomy, Inc. under NASA contract NAS 5-26555. This funding is associated with HST Theory Program AR-17547. A.M.B. acknowledges support from NASA Grant 80NSSC24K0894 and FI-CCA-Research-00011826 from the Simons Foundation.

References

Agertz, O., & Kravtsov, A. V. 2015, ApJ, 804, 18
Agertz, O., Pontzen, A., Read, J. I., et al. 2020, MNRAS, 491, 1656
Akeson, R., Armus, L., Bachelet, E., et al. 2019, arXiv e-prints [arXiv:1902.05569]
Applebaum, E., Brooks, A. M., Christensen, C. R., et al. 2021, ApJ, 906, 96
Arjona-Gálvez, E., Di Cintio, A., & Grand, R. J. J. 2024, A&A, 690, A286
Asplund, M., Grevesse, N., Sauval, A. J., & Scott, P. 2009, Annu. Rev. Astron. Astrophys., 47, 481
Azartash-Namin, B., Engelhardt, A., Munshi, F., et al. 2024, ApJ, 970, 40
Baumschlager, B., Shen, S., & Wadsley, J. W. 2024, A&A, 691, A219
Behroozi, P. S., Wechsler, R. H., & Conroy, C. 2013, ApJ, 770, 57
Bordoloi, R., Tumlinson, J., Werk, J. K., et al. 2014, ApJ, 796, 136
Borrow, J., Kannan, R., Garaldi, E., et al. 2023, MNRAS, 525, 5932
Bose, S., Frenk, C. S., Jenkins, A., et al. 2019, MNRAS, 486, 4790
Boylan-Kolchin, M., Bullock, J. S., & Kaplinghat, M. 2011, MNRAS, 415, L40
Boylan-Kolchin, M., Bullock, J. S., & Kaplinghat, M. 2012, MNRAS, 422, 1203
Brooks, A. M., & Zolotov, A. 2014, ApJ, 786, 87
Brook, C. B., Governato, F., Roškar, R., et al. 2011, MNRAS, 415, 1051
Brook, C. B., Di Cintio, A., Knebe, A., et al. 2014, ApJ, 784, L14
Brown, T. M., Tumlinson, J., Geha, M., et al. 2014, ApJ, 796, 91
Bullock, J. S., Kravtsov, A. V., & Weinberg, D. H. 2000, ApJ, 539, 517
Burchett, J. N., Tripp, T. M., Bordoloi, R., et al. 2016, ApJ, 832, 124
Burkert, A. 2015, ApJ, 808, 158
Christensen, C., Quinn, T., Governato, F., et al. 2012, MNRAS, 425, 3058
Corral van Damme, C., Prod'Homme, T., Isaak, K., Rühl, T., & Sirianni, M. 2024, SPIE Conf. Ser., 13092, 130920Q
Dashyan, G., Silk, J., Mamon, G. A., Dubois, Y., & Hartwig, T. 2018, MNRAS, 473, 5698
de Blok, W. J. G., & Bosma, A. 2002, A&A, 385, 816
Decataldo, D., Shen, S., Mayer, L., Baumschlager, B., & Madau, P. 2024, A&A, 685, A8
Deng, Y., Li, H., Liu, B., et al. 2024, A&A, 691, A231
Dijkstra, M., Haiman, Z., Rees, M. J., & Weinberg, D. H. 2004, ApJ, 601, 666

Donato, F., Gentile, G., Salucci, P., et al. 2009, MNRAS, 397, 1169
Efstathiou, G. 1992, MNRAS, 256, 43
El-Badry, K., Ostriker, E. C., Kim, C.-G., Quataert, E., & Weisz, D. R. 2019, MNRAS, 490, 1961
Emerick, A., Bryan, G. L., & Mac Low, M.-M. 2018, ApJ, 865, L22
Euclid Collaboration (Mellier, Y., et al.) 2025, A&A, 697, A1
Fabian, A. C. 2012, ARA&A, 50, 455
Ferland, G. J., Chatzikos, M., Guzmán, F., et al. 2017, Rev. Mexicana Astron. Astrofis., 53, 385
Fitts, A., Boylan-Kolchin, M., Elbert, O. D., et al. 2017, MNRAS, 471, 3547
Fitts, A., Boylan-Kolchin, M., Bozek, B., et al. 2019, MNRAS, 490, 962
Flores, R. A., & Primack, J. R. 1994, ApJ, 427, L1
Fu, S. W., Weisz, D. R., Starkenburg, E., et al. 2023, ApJ, 958, 167
Garrison-Kimmel, S., Boylan-Kolchin, M., Bullock, J. S., & Lee, K. 2014, MNRAS, 438, 2578
Gnedin, N. Y. 2014, ApJ, 793, 29
Gnedin, N. Y., & Hollon, N. 2012, ApJS, 202, 13
Górski, K. M., Hivon, E., Banday, A. J., et al. 2005, ApJ, 622, 759
Governato, F., Brook, C., Mayer, L., et al. 2010, Nature, 463, 203
Governato, F., Zolotov, A., Pontzen, A., et al. 2012, MNRAS, 422, 1231
Governato, F., Weisz, D., Pontzen, A., et al. 2015, MNRAS, 448, 792
Grond, J. J., Woods, R. M., Wadsley, J. W., & Couchman, H. M. P. 2019, MNRAS, 485, 3681
Gutcke, T. A., Pakmor, R., Naab, T., & Springel, V. 2021, MNRAS, 501, 5597
Gutcke, T. A., Pakmor, R., Naab, T., & Springel, V. 2022a, MNRAS, 513, 1372
Gutcke, T. A., Pfrommer, C., Bryan, G. L., et al. 2022b, ApJ, 941, 120
Haardt, F., & Madau, P. 2012, ApJ, 746, 125
Holguin, F., Hayward, C. C., Ma, X., Anglés-Alcázar, D., & Cochrane, R. K. 2024, arXiv e-prints [arXiv:2405.13110]
Hopkins, P. F., Grudić, M. Y., Wetzel, A., et al. 2020, MNRAS, 491, 3702
Hopkins, P. F., Wetzel, A., Wheeler, C., et al. 2023, MNRAS, 519, 3154
Hu, C.-Y., Naab, T., Walch, S., Glover, S. C. O., & Clark, P. C. 2016, MNRAS, 458, 3528
Hu, C.-Y., Smith, M. C., Teyssier, R., et al. 2023, ApJ, 950, 132
Ivezić, Ž., Kahn, S. M., Tyson, J. A., et al. 2019, ApJ, 873, 111
Jeon, M., Besla, G., & Bromm, V. 2017, ApJ, 848, 85
Jethwa, P., Erkal, D., & Belokurov, V. 2018, MNRAS, 473, 2060
Johnson, S. D., Chen, H.-W., Mulchaey, J. S., Schaye, J., & Straka, L. A. 2017, ApJ, 850, L10
Kannan, R., Garaldi, E., Smith, A., et al. 2022, MNRAS, 511, 4005
Karukes, E. V., & Salucci, P. 2017, MNRAS, 465, 4703
Katz, H. 2022, MNRAS, 512, 348
Katz, H., Ramsoy, M., Rosdahl, J., et al. 2020, MNRAS, 494, 2200
Keller, B. W., Wadsley, J., Benincasa, S. M., & Couchman, H. M. P. 2014, MNRAS, 442, 3013
Kimm, T., & Cen, R. 2014, ApJ, 788, 121
Kim, C.-G., & Ostriker, E. C. 2017, ApJ, 846, 133
Kirby, E. N., Lanfranchi, G. A., Simon, J. D., Cohen, J. G., & Guhathakurta, P. 2011, ApJ, 727, 78
Kirby, E. N., Cohen, J. G., Guhathakurta, P., et al. 2013, ApJ, 779, 102
Klypin, A., Kravtsov, A. V., Valenzuela, O., & Prada, F. 1999, ApJ, 522, 82
Koudmani, S., Henden, N. A., & Sijacki, D. 2021, MNRAS, 503, 3568
Koudmani, S., Rennehan, D., Somerville, R. S., et al. 2025, MNRAS, 540, 1928
Kroupa, P. 2001, MNRAS, 322, 231
Leitherer, C., Ekström, S., Meynet, G., et al. 2014, ApJS, 212, 14
Leung, S.-C., & Nomoto, K. 2018, ApJ, 861, 143
Li, F., Rahman, M., Murray, N., et al. 2021, MNRAS, 500, 1038
Liang, C. J., & Chen, H.-W. 2014, MNRAS, 445, 2061
Macciò, A. V., Frings, J., Buck, T., et al. 2017, MNRAS, 472, 2356
Madau, P., Kuhlen, M., Diemand, J., et al. 2008, ApJ, 689, L41
Madau, P., Shen, S., & Governato, F. 2014, ApJ, 789, L17
Marleau, F. R., Cuillandre, J.-C., Cantiello, M., et al. 2025, A&A, 697, A12
Martin-Alvarez, S., Sijacki, D., Haehnelt, M. G., et al. 2023, MNRAS, 525, 3806
Mashchenko, S., Wadsley, J., & Couchman, H. M. P. 2008, Science, 319, 174
McConnachie, A. W. 2012, AJ, 144, 4
McQuinn, K. B. W., B. Newman, M. J., Savino, A., et al. 2024, ApJ, 961, 16
Mina, M., Shen, S., Keller, B. W., et al. 2021, A&A, 655, A22
Mina, M., Mota, D. F., & Winther, H. A. 2022, A&A, 662, A29
Mishra, N., Johnson, S. D., Rudie, G. C., et al. 2024, ApJ, 976, 149
Moore, B., Ghigna, S., Governato, F., et al. 1999, ApJ, 524, L19
Moster, B. P., Naab, T., & White, S. D. M. 2013, MNRAS, 428, 3121
Mostow, O., Torrey, P., Rose, J. C., et al. 2025, ApJ, 995, 25
Muni, C., Pontzen, A., Read, J. I., et al. 2025, MNRAS, 536, 314
Munshi, F., Brooks, A. M., Christensen, C., et al. 2019, ApJ, 874, 40
Munshi, F., Brooks, A. M., Applebaum, E., et al. 2021, ApJ, 923, 35
Nadler, E. O., Wechsler, R. H., Bechtol, K., et al. 2020, ApJ, 893, 48
Navarro, J. F., Eke, V. R., & Frenk, C. S. 1996, MNRAS, 283, L72
Nelson, D., Sharma, P., Pillepich, A., et al. 2020, MNRAS, 498, 2391
Nori, M., Bhatia, S., & Macciò, A. V. 2024, arXiv e-prints [arXiv:2411.09733]
Oñorbe, J., Boylan-Kolchin, M., Bullock, J. S., et al. 2015, MNRAS, 454, 2092
Obreja, A., Arrigoni Battaia, F., Macciò, A. V., & Buck, T. 2024, MNRAS, 527, 8078
Oppenheimer, B. D., Segers, M., Schaye, J., Richings, A. J., & Crain, R. A. 2018, MNRAS, 474, 4740
Orkney, M. D. A., Read, J. I., Rey, M. P., et al. 2021, MNRAS, 504, 3509
Papaderos, P., Guseva, N. G., Izotov, Y. I., & Fricke, K. J. 2008, A&A, 491, 113
Peñarrubia, J., Pontzen, A., Walker, M. G., & Koposov, S. E. 2012, ApJ, 759, L42
Peters, T., Naab, T., Walch, S., et al. 2017, MNRAS, 466, 3293
Piacitelli, D. R., Brooks, A. M., Christensen, C., et al. 2025, ApJ, 993, 230
Pignatari, M., Herwig, F., Hirschi, R., et al. 2016, ApJS, 225, 24
Pontzen, A., & Governato, F. 2012, MNRAS, 421, 3464
Power, C., Navarro, J. F., Jenkins, A., et al. 2003, MNRAS, 338, 14
Prochaska, J. X., Weiner, B., Chen, H. W., Mulchaey, J., & Cooksey, K. 2011, ApJ, 740, 91
Prochaska, J. X., Werk, J. K., Worseck, G., et al. 2017, ApJ, 837, 169
Putman, M. E., Zheng, Y., Price-Whelan, A. M., et al. 2021, ApJ, 913, 53
Raiteri, C. M., Villata, M., & Navarro, J. F. 1996, A&A, 315, 105
Read, J. I., & Erkal, D. 2019, MNRAS, 487, 5799
Read, J. I., & Gilmore, G. 2005, MNRAS, 356, 107
Read, J. I., Iorio, G., Agertz, O., & Fraternali, F. 2017, MNRAS, 467, 2019
Read, J. I., Walker, M. G., & Steger, P. 2019, MNRAS, 484, 1401
Revaz, Y., & Jablonka, P. 2018, A&A, 616, A96
Rey, M. P., Taylor, E., Gray, E. I., et al. 2025, MNRAS, 541, 1195
Richings, A. J., Schaye, J., & Oppenheimer, B. D. 2014, MNRAS, 440, 3349
Richstein, H., Kallivayalil, N., Simon, J. D., et al. 2024, ApJ, 967, 72
Rosdahl, J., Schaye, J., Teyssier, R., & Agertz, O. 2015, MNRAS, 451, 34
Rosdahl, J., Katz, H., Blaizot, J., et al. 2018, MNRAS, 479, 994
Salucci, P. 2019, A&A Rev., 27, 2
Salucci, P., Wilkinson, M. I., Walker, M. G., et al. 2012, MNRAS, 420, 2034
Santos-Santos, I. M., Di Cintio, A., Brook, C. B., et al. 2018, MNRAS, 473, 4392
Sawala, T., Frenk, C. S., Fattahi, A., et al. 2016, MNRAS, 457, 1931
Scannapieco, C., Wadepuhl, M., Parry, O. H., et al. 2012, MNRAS, 423, 1726
Schaye, J., Crain, R. A., Bower, R. G., et al. 2015, MNRAS, 446, 521
Schmidt, M. 1959, ApJ, 129, 243
Sellwood, J. A., & McGaugh, S. S. 2005, ApJ, 634, 70
Sharma, R. S., Brooks, A. M., Somerville, R. S., et al. 2020, ApJ, 897, 103
Sharma, R. S., Brooks, A. M., Tremmel, M., Bellovary, J., & Quinn, T. R. 2023, ApJ, 957, 16
Shen, S., Wadsley, J., & Stinson, G. 2010, MNRAS, 407, 1581
Shen, S., Madau, P., Aguirre, A., et al. 2012, ApJ, 760, 50
Shen, S., Madau, P., Guedes, J., et al. 2013, ApJ, 765, 89
Shen, S., Madau, P., Conroy, C., Governato, F., & Mayer, L. 2014, ApJ, 792, 99
Shen, X., Hopkins, P. F., Necib, L., et al. 2024, ApJ, 966, 131
Simon, J. D. 2019, ARA&A, 57, 375
Smith, M. C., Sijacki, D., & Shen, S. 2018, MNRAS, 478, 302
Smith, M. C., Sijacki, D., & Shen, S. 2019, MNRAS, 485, 3317
Smith, M. C., Bryan, G. L., Somerville, R. S., et al. 2021, MNRAS, 506, 3882
Stinson, G., Seth, A., Katz, N., et al. 2006, MNRAS, 373, 1074
Strawn, C., Roca-Fàbrega, S., Primack, J. R., et al. 2024, ApJ, 962, 29
Tolstoy, E., Hill, V., & Tosi, M. 2009, ARA&A, 47, 371
Verner, D. A., Ferland, G. J., Korista, K. T., & Yakovlev, D. G. 1996, ApJ, 465, 487
Vogelsberger, M., Zavala, J., Simpson, C., & Jenkins, A. 2014, MNRAS, 444, 3684
Wadsley, J. W., Keller, B. W., & Quinn, T. R. 2017, MNRAS, 471, 2357
Wadsley, J. W., Baumschlager, B., & Shen, S. 2024, MNRAS, 528, 3767
Walch, S., & Naab, T. 2015, MNRAS, 451, 2757
Weisz, D. R., Dolphin, A. E., Skillman, E. D., et al. 2014, ApJ, 789, 147
Werk, J. K., Prochaska, J. X., Thom, C., et al. 2013, ApJS, 204, 17
Wetzel, A. R., Hopkins, P. F., Kim, J.-h., et al. 2016, ApJ, 827, L23
Wheeler, C., Oñorbe, J., Bullock, J. S., et al. 2015, MNRAS, 453, 1305
Wheeler, C., Hopkins, P. F., Pace, A. B., et al. 2019, MNRAS, 490, 4447
Wolfe, A. M., Gawiser, E., & Prochaska, J. X. 2005, ARA&A, 43, 861
Wright, A. C., Brooks, A. M., Weisz, D. R., & Christensen, C. R. 2019, MNRAS, 482, 1176
Zhang, E., Sales, L. V., Marinacci, F., et al. 2024, ApJ, 975, 229
Zheng, Y., Emerick, A., Putman, M. E., et al. 2020, ApJ, 905, 133
Zheng, Y., Faerman, Y., Oppenheimer, B. D., et al. 2024, ApJ, 960, 55
Zhu, B., & Springel, V. 2024, MNRAS, 533, 4360
Zolotov, A., Brooks, A. M., Willman, B., et al. 2012, ApJ, 761, 71